

Internal gravity waves in stratified flows with and without vortical modes

Vincent Labarre,^{1,*} Pierre Augier,^{2,†} Giorgio Krstulovic,^{1,‡} and Sergey Nazarenko^{3,§}

¹*Université Côte d'Azur, Observatoire de la Côte d'Azur, CNRS, Laboratoire Lagrange, Nice, France.*

²*Laboratoire des Écoulements Géophysiques et Industriels,*

Université Grenoble Alpes, CNRS, Grenoble-INP, F-38000 Grenoble, France

³*Université Côte d'Azur, CNRS, Institut de Physique de Nice - INPHYNI, Nice, France*

The comprehension of stratified flows is important for geophysical and astrophysical applications. The Weak Wave Turbulence theory aims to provide a statistical description of internal gravity waves propagating in the bulk of such flows. Yet, internal gravity waves are usually perturbed by other structures present in stratified flow, namely the shear modes and the vortical modes. In order to check whether a weak internal gravity wave turbulence regime can occur, we perform direct numerical simulations of stratified turbulence without shear modes, and with or without vortical modes at various Froude and buoyancy Reynolds numbers. We observe that removing vortical modes naturally helps to have a better overall balance between poloidal kinetic energy, involved in internal gravity waves, and potential energy. However, conversion between kinetic energy and potential energy do not necessarily show fluctuations around zero in our simulations, as we would expect for a system of statistically stationary waves. A spatiotemporal analysis reveals that removing vortical modes helps to concentrate the energy around the wave frequency, but it is not enough to observe a wave turbulence regime. Yet, we observe that internal gravity waves whose frequency are large compared to the eddy turnover time are present, and we also find evidences for slow internal gravity waves interacting by Triadic Resonance Instabilities in our strongly stratified flows simulations.

I. INTRODUCTION

As eddies in classical hydrodynamic turbulence, waves in nonlinear systems interact and transfer conserved quantities along scales in a cascade process. The Weak-Wave Turbulence (WWT) theory aims to provides a statistical description of the system when the non-linearity is small [1–3]. The applications of this theory encompass capillary-gravity waves [4], Alfvén waves in magnetohydrodynamics (MHD) [5], inertial and internal waves in rotating and stratified fluids [6–8], Kelvin waves in superfluids [9], elastic plates [10], gravitational waves [11], density waves in Bose-Einstein condensates [12], or 2D acoustic waves [13].

Two key hypotheses are used in WWT. The first one is weak non-linearity of the dynamical equations. This condition is often translated in terms of the separation of spatial scales: the considered scale on one side and the saturation scale on the other side. The saturation scale is here defined as the scale at which the weak non-linearity does not holds anymore, inducing wave breaking. This hypothesis is quite similar to the separation between the integral scale and the dissipative scale in the classical picture of three-dimensional hydrodynamic turbulence. The second hypothesis corresponds to a time scales separation, and is more specific to WWT. It requires that the linear time, given by the wave period τ_L , is small compared to the non-linear time of interactions between waves τ_{NL} [2].

For many physical systems, at least one the two hypotheses is broken in some range of scales, which reduce or even break the validity of WWT [14]. Yet, when scales separations are observed in space and time, a weak wave turbulent range can appear in spatiotemporal spectra of waves' energy. Besides experimental and numerical difficulties for obtaining scales' separations, testing WWT in isotropic systems is conceptually simpler. For this reason, many progress have been made in the experimental and numerical verification of WWT for elastic plates [15, 16], capillary-gravity waves [4, 17], density waves in Bose-Einstein condensates [18], or 2D acoustic waves [13].

Anisotropic turbulence is, generally speaking, more difficult to investigate due to the reduce number of symmetries of the considered flows. For example, it has been shown that studying two-dimensional spatial spectra instead of one-dimensional integrated spectra is essential to investigate stratified turbulence [19]. Then, the anisotropy makes the problem multidimensional in Fourier space, which makes the notion of spectral energy fluxes more difficult than in isotropic turbulence [20]. An additional difficulty is that scales separations required by WWT can also be anisotropic.

* vincent.labarre@oca.eu

† pierre.augier@univ-grenoble-alpes.fr

‡ giorgio.krstulovic@oca.eu

§ sergey.nazarenko@unice.fr

For linearly stratified flows, weak non-linearity of the Navier-Stokes equations requires the spatial scale's separation

$$k/k_b \ll 1, \quad (1)$$

where $k_b = N/U_h$ is the buoyancy wave-vector, k is the wave-vector modulus, U_h is the rms of the horizontal velocity, and N is the Brunt-Väisälä frequency. This condition should be fulfilled in order to avoid wave-breaking. The temporal scale separation between linear waves and eddies leads to the different condition

$$\tau_L/\tau_{NL} = \frac{(\varepsilon_{\text{kin}}k^2)^{1/3}}{Nk_h/k} \ll 1, \quad (2)$$

where ε_{kin} is the kinetic energy dissipation rate, k_h is the horizontal wave-vector modulus, $\tau_L = 2\pi k/(Nk_h)$ is the period of the linear waves, and $\tau_{NL} = 2\pi/(k^2\varepsilon_{\text{kin}})^{1/3}$ is the eddy turnover time. Physically, when $\chi_L \ll 1$, the waves are faster than the typical time of their non-linear interactions. Due to the anisotropic dispersion relation of internal gravity waves, time scales separation will be less valid for small k_h , and even impossible for modes with $k_h = 0$. Consequently, separation of times scales can be violated even if a large separation of spatial scales is observed (i.e. $k/k_b \ll 1$). It is therefore more difficult to observe signatures of wave turbulence in anisotropic systems like MHD, or rotating and stratified flows.

Stratified flows are not only an interesting conceptual problem, but they are also important for the understanding of geophysical flows [21, 22]. In particular, understanding the role of waves in mixing is required for sub-grid parameterizations in climate models [23, 24]. It is therefore not surprising that stratified flows received a particular attention from both the “strong” turbulence community [25–35], and the WWT community [6, 9, 36–38]. It turns out that internal waves are effectively important in the dynamics and mixing in stratified flows [39–41], and that, three-wave resonant interactions are responsible for slow, net energy transfers between different wave-numbers [42–44]. Internal waves can be excited, for example, by tides [45] or by linearly unstable waves attractor [42]. However, many questions and issues remain about the applicability of WWT to stratified flows.

A recent study, [19], showed that a wave dominated region should lie in the spectral region defined by $\tau_L/\tau_{NL} < 1/3$, in agreement with observations made for MHD [46]. Yet, non-waves structures like shear modes (purely vertical shear) and vortical modes (vertical vorticity) still make the observation of a system of weakly interacting internal gravity waves delicate. The same problem appear in rotating flows, in which the geostrophic modes plays the role of the non-propagative structure. It has been ingeniously shown that tidal forcing is very efficient at triggering weakly nonlinear internal gravity waves [45], in a way reminiscent of the inertial waves' excitation by libration in rotating fluids [47, 48]. Yet, interactions with the base flows remains [45, 47]. Experimentalists bypassed this difficulty to observe weak inertial wave turbulence in a rotating tank, by using honeycomb grids at top and bottom boundaries to dissipate geostrophic modes efficiently [49, 50], in a similar fashion to the numerical study of [47]. These works point out that some waves systems have a tendency to generate non-wave motions that can severely affect the waves' dynamics and should be suppressed in experiments aiming to observe wave turbulence. In rotating flows these modes are geostrophic flows, while in stratified flows these modes are vertical shear and vertical vorticity [51].

The most commonly used WWT prediction is certainly the scale invariant stationary solutions to the kinetic equation, which gives the expected spatial waves' energy spectra in the statistically steady state. The solutions are usually of two types: the thermodynamic equilibrium solution (Rayleigh-Jeans spectra), and the non equilibrium solution(s) that are linked to the cascade(s) of the dynamical invariant(s) of the system among scales (Kolmogorov-Zakharov spectra) [2]. It is important to note that these solutions can be considered as valid only if the collision integral in the waves' kinetic equation converges. The importance of the nonlinear interactions among internal gravity waves was recognized early, leading to several derivations of waves' kinetic equations (see [52, 53]). Derivation of the Kolmogorov-Zakharov spectra in the limit of large vertical wave-numbers $k_z \simeq k \gg k_h$ can be found in [6, 36]. This solution corresponds to an energy cascade, and is given by the energy spectra

$$E(k_h, k_z) \sim k_h^{-5/2} k_z^{-3/2}. \quad (3)$$

Yet, it was noted that this solution comes through a spurious cancellation between oppositely signed divergent contributions in their respective collision integrals. Therefore, the existence of this solution is fortuitous. Later, it was shown that power law solutions $n(k_h, k_z) \sim k_h^{-\alpha_h} k_z^{-\alpha_z}$ have convergent collision integral's contributions only on the segment $\alpha_h \in]3, 4[$, $\alpha_z = 0$ [37, 54]. The collision integral was then computed numerically for $\alpha_z = 0$, and it was

deduced that the only scale invariant stationary solution to the kinetic equation (zero of the collision integral) was close to

$$E(k_h, k_z) \sim k_h^{-2.69} k_z^{-1}. \quad (4)$$

It was also shown that, on the segment $\alpha_z = 0$, the dominant contributions to the collision integral corresponds to non-local transfers first identified by McComas [55], notably the Parametric Subharmonic Instability (PSI) [52, 55] observed in oceans [56] and experiments [44], consisting in the resonant interaction of a primary wave and two smaller-scale waves of nearly half the frequency.

The present study first deals with the existence and properties of a weak internal gravity waves turbulence regime. To this end, we perform numerical simulations of stratified turbulence at various stratifications and viscosity. In the same spirit than experiments in a rotating tank presented in [49, 50], we removed shear modes in all of our simulations. For each values of the control parameters, we performed two “twins” simulations: one where the vortical modes remain, and one where vortical modes are removed from the dynamics by a projection in spectral space [57]. Note that, in order to get rid of non waves structures, numerical simulations of reduced dynamical equations (i.e. without non-waves structures) of stratified rotating flows in the hydrostatic balance where already done [58]. Despite the simplifications, these simulations reproduced some key features of oceanic internal-wave spectra: accumulation of energy at near-inertial waves and realistic frequency and horizontal wave-number dependencies of spatiotemporal spectra. In the present work, we do not account for rotation, and do not use the hydrostatic balance approximation. Also, having twins simulations (i.e. with or without vortical modes) allows to have a better comparison to understand the role of the vortical modes on the dynamics of stratified flows.

The manuscript is organized as follows. In section II, we present our methodology including a presentation of the code and the simulations. Our results are presented in section III. Subsection III A is devoted to the study of flow regimes and global energy ratios in the control parameters space for our simulations. It allows us to observe that WWT is naturally more likely to occurs at high stratification and without vortical modes. Subsections III B and III C deal with the spatiotemporal analysis of a couple of strongly stratified simulations in order to investigate further the presence of linear waves in spatial scales. In the last subsection III D, we propose a simple diagnostic to evaluate the predominancy of waves in the parameter space. We give concluding remarks in section IV.

II. METHODS

We start from the three-dimensional Navier-Stokes equations under the Boussinesq approximation with added hyper-viscous hyperdiffusion terms:

$$\nabla \cdot \mathbf{v} = 0 \quad (5)$$

$$\partial_t \mathbf{v} + \mathbf{v} \cdot \nabla \mathbf{v} = b \mathbf{e}_z - \nabla p + \nu \nabla^2 \mathbf{v} - \nu_4 \nabla^4 \mathbf{v} + \mathbf{f}, \quad (6)$$

$$\partial_t b + \mathbf{v} \cdot \nabla b = -N^2 v_z + \kappa \nabla^2 b - \kappa_4 \nabla^4 b, \quad (7)$$

where $\mathbf{r} = (x, y, z)$ will represent the three spatial coordinates in the cartesian frame $(O, \mathbf{e}_x, \mathbf{e}_y, \mathbf{e}_z)$, \mathbf{e}_z is the stratification axis, $\mathbf{v} = (v_x, v_y, v_z)$ is the velocity, b the buoyancy, p the total kinematic pressure, N the Brunt-Väisälä frequency, ν the viscosity, κ the diffusivity, ν_4 the hyperviscosity, κ_4 the hyperdiffusivity, and \mathbf{f} is the velocity forcing. In this study, we fix the Schmidt number $Sc = \nu/\kappa$ to one. We consider a periodic domain of horizontal size $L_x = L_y = L_h = 3$. The vertical size of the domain, L_z , is varied depending on the stratification. We note (n_x, n_y, n_z) the numbers of collocations points in the three spatial directions, with $n_x = n_y \equiv n_h$.

The Fourier transform of the velocity field $\hat{\mathbf{v}}_{\mathbf{k}} = (\hat{v}_x, \hat{v}_y, \hat{v}_z)$ can be written using the commonly used poloidal-toroidal-shear decomposition (see e.g. [31, 35, 57, 59–61])

$$\hat{\mathbf{v}}_{\mathbf{k}} = \begin{cases} \hat{v}_{p\mathbf{k}} \mathbf{e}_{p\mathbf{k}} + \hat{v}_{t\mathbf{k}} \mathbf{e}_{t\mathbf{k}} & \text{if } k_h \neq 0, \\ \hat{v}_{s\mathbf{k}} = \hat{v}_x \mathbf{e}_x + \hat{v}_y \mathbf{e}_y & \text{if } k_h = 0. \end{cases} \quad (8)$$

where

$$\mathbf{e}_{\mathbf{k}} = \frac{\mathbf{k}}{k}, \quad \mathbf{e}_{p\mathbf{k}} = \frac{\mathbf{k} \times (\mathbf{k} \times \mathbf{e}_z)}{|\mathbf{k} \times (\mathbf{k} \times \mathbf{e}_z)|}, \quad \mathbf{e}_{t\mathbf{k}} = \frac{\mathbf{e}_z \times \mathbf{k}}{|\mathbf{e}_z \times \mathbf{k}|}, \quad (9)$$

$\hat{v}_{p\mathbf{k}}$ is the poloidal velocity, $\hat{v}_{t\mathbf{k}}$ is the toroidal velocity, $\hat{v}_{s\mathbf{k}}$ is the shear modes velocity, $\mathbf{k} = (k_x, k_y, k_z)$ denotes the wave-vector, $k = |\mathbf{k}| = \sqrt{k_x^2 + k_y^2 + k_z^2}$ is its modulus, and $k_h = \sqrt{k_x^2 + k_y^2}$ is the modulus of the horizontal component

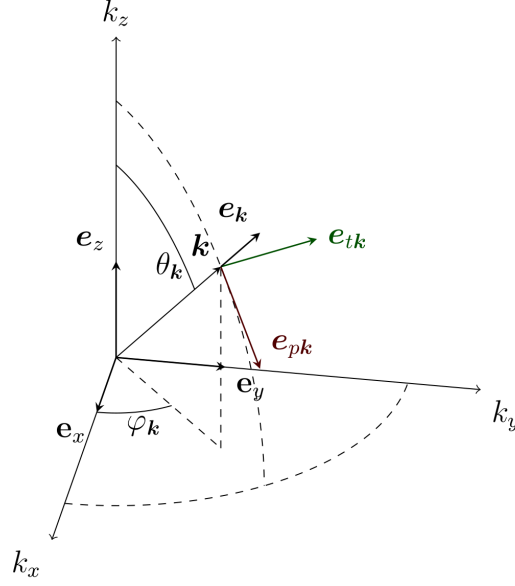


FIG. 1. Illustration of the poloidal-toroidal basis $(\mathbf{e}_k, \mathbf{e}_{pk}, \mathbf{e}_{tk})$ defined by equations (9). θ_k is the angle between \mathbf{e}_z and \mathbf{e}_k . φ_k is the angle between the horizontal projection of \mathbf{k} and \mathbf{e}_x .

of the wave-vector (Figure 1).

In spectral space, once projected, the equations of motion (5-7) then reads

$$\begin{cases} \dot{\hat{v}}_{pk} &= -(\widehat{\mathbf{v} \cdot \nabla \mathbf{v}})_k \cdot \mathbf{e}_{pk} - \hat{b}_k \sin \theta_k - \nu k^2 \hat{v}_{pk} - \nu_A k^4 \hat{v}_{pk} + \hat{\mathbf{f}}_k \cdot \mathbf{e}_{pk}, \\ \dot{\hat{v}}_{tk} &= -(\widehat{\mathbf{v} \cdot \nabla \mathbf{v}})_k \cdot \mathbf{e}_{tk} - \nu k^2 \hat{v}_{tk} - \nu_A k^4 \hat{v}_{tk} + \hat{\mathbf{f}}_k \cdot \mathbf{e}_{tk}, \\ \dot{\hat{b}}_k &= -(\widehat{\mathbf{v} \cdot \nabla b})_k + N^2 \hat{v}_{pk} \sin \theta_k - \kappa k^2 \hat{b}_k - \kappa_A k^4 \hat{b}_k \end{cases} \quad (10)$$

if $k_h \neq 0$, and

$$\begin{cases} \dot{\hat{v}}_{sk} &= -(\widehat{\mathbf{v} \cdot \nabla \mathbf{v}_h})_k - \nu k^2 \hat{v}_{sk} - \nu_A k^4 \hat{v}_{sk}, \\ \dot{\hat{b}}_k &= -(\widehat{\mathbf{v} \cdot \nabla b})_k - \kappa k^2 \hat{b}_k - \kappa_A k^4 \hat{b}_k \end{cases} \quad (11)$$

if $k_h = 0$, where $\mathbf{v}_h = (v_x, v_y, 0)$ is the horizontal component of \mathbf{v} and $(\widehat{\cdot})_k$ denotes the Fourier transform. We will also note $k_i \in \delta k_i \mathbb{Z}$ with $\delta k_i = 2\pi/L_i$ for $i = x, y, z$, and $\delta k_x = \delta k_y \equiv \delta k_h$.

The linear, unforced, inviscid dynamics can be written as

$$\dot{a}_k^{(-)} = -i\omega_k a_k^{(-)}, \quad \dot{a}_k^{(0)} = 0, \quad \dot{a}_k^{(+)} = +i\omega_k a_k^{(+)} \quad \text{if } k_h \neq 0 \quad (12)$$

$$\dot{\hat{v}}_{sk} = \mathbf{0}, \quad \dot{\hat{b}}_k = 0 \quad \text{if } k_h = 0. \quad (13)$$

where $a_k^\pm = (\hat{v}_{pk} \pm i \frac{\hat{b}_k}{N}) / \sqrt{2\omega_k}$ are the waves modes,

$$\omega_k = N k_h / k = N \sin \theta_k \quad (14)$$

is the pulsation of the waves, θ_k is the angle between \mathbf{k} and the stratification axis \mathbf{e}_z , and $a_k^{(0)} = \hat{v}_{tk}$ are the vortical modes (corresponding to vertical vorticity). Equations (12-13) show that both shear modes and vortical modes have zero frequency. It is then clear that linear waves live in the poloidal velocity and the buoyancy, but not in the toroidal velocity nor the shear velocity.

Since we are motivated by forcing internal gravity waves, in which only the poloidal part is involved and whose dispersion relation is anisotropic, we use an anisotropic, poloidal velocity forcing $\hat{\mathbf{f}}_k = \hat{f}_k \mathbf{e}_{pk}$. The flow is forced at

large spatial scales and small angle $\{\mathbf{k} \mid 5 \leq k/\delta k_h \leq 20, |\omega_{\mathbf{k}}(\mathbf{k})/N - \sin \theta_f| \leq 0.05\}$ where $\sin \theta_f = 0.3$, meaning that relatively slow internal waves are forced. The correlation time of the forcing is equal to the period of the forced waves $T_c = 2\pi/(N \sin \theta_f)$. It is computed in spectral space such that the kinetic energy injection rate P_K is constant and equal to unity. The forcing scheme is described by the algorithm given in appendix A. All modes with wavenumber modulus larger than $k_{\max} = 0.8(n_h/2)\delta k_h$ are truncated to limit aliasing. Shear modes and vertically invariant vertical velocity (internal waves at $\omega = N$), which are absent in flows bounded by walls, are also removed in our simulations.

We add hyperviscosity and hyperdiffusivity terms of order 4, $\nu_4 = \kappa_4$, in many simulations in order to enlarge the inertial range. We measure the turbulent kinetic dissipations ε_{K2} and ε_{K4} based on both viscosities, and the total kinetic energy dissipation $\varepsilon_{\text{kin}} = \varepsilon_{K2} + \varepsilon_{K4}$. The product of the maximal wave-vector k_{\max} with the Kolmogorov scales $\eta \equiv (\nu^3/\varepsilon_{K2})^{1/4}$ is computed. The time advancement is performed using the 4th order Runge-Kutta scheme. The numerical simulations are performed using the pseudo-spectral solver `ns3d.strat` from the FluidSim Python package [62].

The turbulent non-dimensional numbers characterizing the flow are the horizontal turbulent Froude number and the buoyancy Reynolds numbers that are respectively

$$F_h = \frac{\varepsilon_{\text{kin}}}{U_h^2 N} \quad \text{and} \quad \mathcal{R} = \frac{\varepsilon_{\text{kin}}}{\nu N^2}, \quad (15)$$

where ε_{kin} is the average kinetic energy dissipation rate, and U_h is the rms of the horizontal velocity. We also compute the buoyancy and the Ozmidov wave-vectors $k_b \equiv N/U_h$ and $k_O \equiv \sqrt{N^3/\varepsilon_{\text{kin}}}$. All the quantities presented in this manuscript are computed from averaging when stationary is reached. A list of the simulations, with relevant parameters and physical quantities is given by table B.

III. RESULTS

A. Regimes and global energy distribution

In this subsection, we study the anisotropy of the flow and global energy budget in the (F_h, \mathcal{R}) plane. To discuss stratified turbulence regimes, it is useful to introduce a large scale isotropy coefficient and a small scale isotropy coefficient [63]. The former is based on the kinetic energy's components

$$I_{\text{kin}} = \frac{3E_{\text{kin},z}}{E_{\text{kin}}} \quad (16)$$

where $E_{\text{kin},z}$ is the vertical velocity kinetic energy and E_{kin} is the total kinetic energy. The small scale isotropy coefficient is computed using the kinetic energy dissipation rates, namely

$$I_{\text{diss}} = \frac{1 - \varepsilon_{\text{kin},z}/\varepsilon_{\text{kin}}}{(1 - 1/3)} \quad (17)$$

where $\varepsilon_{\text{kin},z}$ is the energy dissipation rate due to vertical gradients. Both I_{kin} and I_{diss} are equal to unity for an isotropic flow. Conversely, I_{kin} and I_{diss} should be close to zero if the flow is strongly anisotropic. When vortical modes are removed, the following definitions are used

$$I_{\text{kin}} = \frac{2E_{\text{kin},z}}{E_{\text{kin}}}, \quad \text{and} \quad I_{\text{diss}} = \frac{1 - \varepsilon_{\text{kin},z}/\varepsilon_{\text{kin}}}{(1 - 1/2)} \quad (18)$$

because it is expected that only half of the kinetic is contained in (respectively dissipated by) the vertical velocity field (respectively the vertical gradients) in this case if the energy spectra are independent of the angles in this case. Figure 2 shows the variations of I_{kin} and I_{diss} with (F_h, \mathcal{R}) . Small points correspond to strong anisotropic energy dissipation while big points correspond to isotropic energy dissipation. Dark points correspond to strong large scale isotropy while light points correspond to isotropic flows. I_{kin} and I_{diss} allow to distinguish between four regimes (Figure 2(a)): the passive scalar regime where $I_{\text{kin}} \simeq 1$, the weakly stratified regime where $0.5 \leq I_{\text{kin}} \leq 1$, and the strongly stratified regimes where $I_{\text{kin}} \leq 0.5$. As explained in [29], the strongly stratified flows fall in two

regimes: The strongly stratified regime where the dissipation is isotropic because a 3D turbulence range can develop, typically when $\mathcal{R} \geq 10$; The viscosity affected regime where the small dissipative scales remain affected by the anisotropy. We observe that removing vortical modes does not modify this picture (Figure 2(b)). However, for a given (F_h, \mathcal{R}) , we observe that the isotropy coefficients tend to have bigger values when the vortical modes are removed.

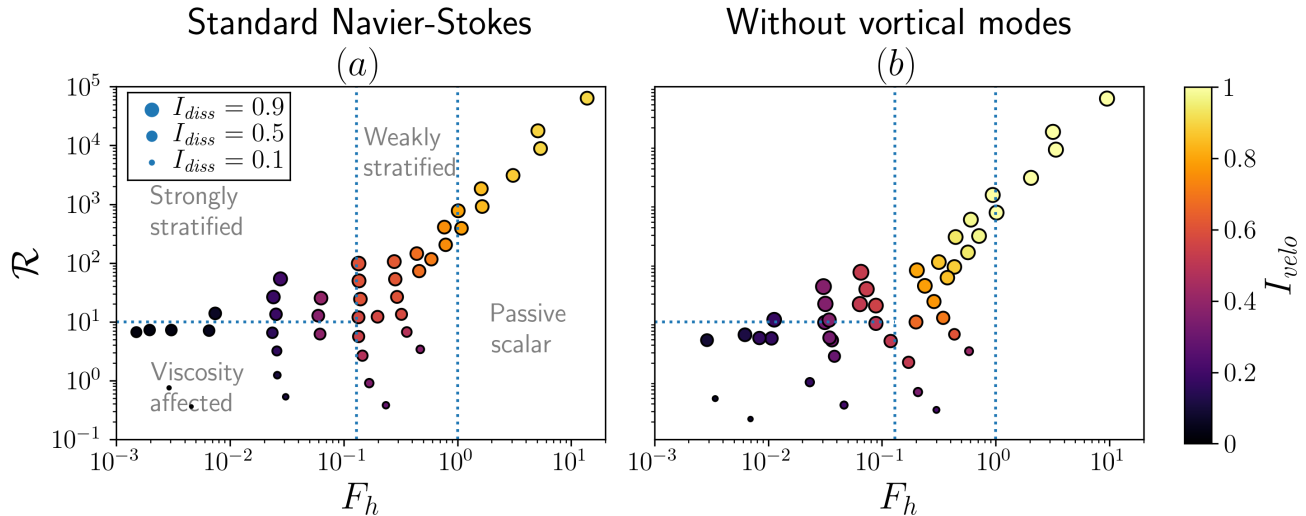


FIG. 2. Classification of regimes in our simulations using the isotropy coefficients. The large scale isotropy coefficient I_{kin} is given by the color-scale, and the small scale isotropy coefficient I_{diss} by the size of the symbols. For simulations with vortical modes (a), definitions (16-17) are used. For simulations without vortical modes (b), definitions (18) are used.

We note

$$E_{\text{pot}} = \frac{1}{2N^2} \sum_{\mathbf{k}} |\hat{b}_{\mathbf{k}}|^2, \quad E_{\text{polo}} = \frac{1}{2} \sum_{\mathbf{k}} |\hat{v}_{p\mathbf{k}}|^2, \quad E_{\text{toro}} = \frac{1}{2} \sum_{\mathbf{k}} |\hat{v}_{t\mathbf{k}}|^2, \quad \tilde{\mathcal{D}} = \frac{E_{\text{polo}} - E_{\text{pot}}}{E_{\text{polo}} + E_{\text{pot}}} \quad (19)$$

which are, respectively, the potential energy, the poloidal kinetic energy, the vortical modes (toroidal) kinetic energy, and the relative difference between poloidal and potential energy. We also note $E = E_{\text{pot}} + E_{\text{polo}} + E_{\text{toro}}$ the total energy. Figure 3 shows the vortical modes energy ratio E_{toro}/E and $\tilde{\mathcal{D}}$ as a function of F_h and \mathcal{R} . For waves, we expect to observe an equipartition between the poloidal kinetic energy and potential energy. Consequently, both E_{toro}/E and $\tilde{\mathcal{D}}$ should be close to zero for a system mainly composed by internal gravity waves. We observe that vortical modes energy becomes dominant at high stratification (low F_h) if they are not removed from the dynamics in these simulations with $\mathcal{R} \geq 0.1$ (Figure 3 (a)). The ratio E_{toro}/E is the lowest at intermediate stratification $F_h \simeq 0.1 - 0.3$ and low values of \mathcal{R} . However, the same simulations are marked by a predominance of potential energy over poloidal energy, $\tilde{\mathcal{D}} < 0$ (Figure 3 (b)), meaning that these weakly stratified flows do contain other structures than waves. When vortical modes are removed, we can obtain flows with a global balance between poloidal and potential energies ($\tilde{\mathcal{D}} \simeq 0$) at high stratification. Consequently, a flow governed by weak non-linear interactions between waves may be obtained at high stratification by removing vortical modes. In the two next subsections, we perform a spatiotemporal analysis of a couple of strongly stratified turbulent simulations with $(N, \mathcal{R}_i \equiv 1/\nu N^2) = (40, 20)$ and aspect ratio $L_z/L_h = 1/4$.

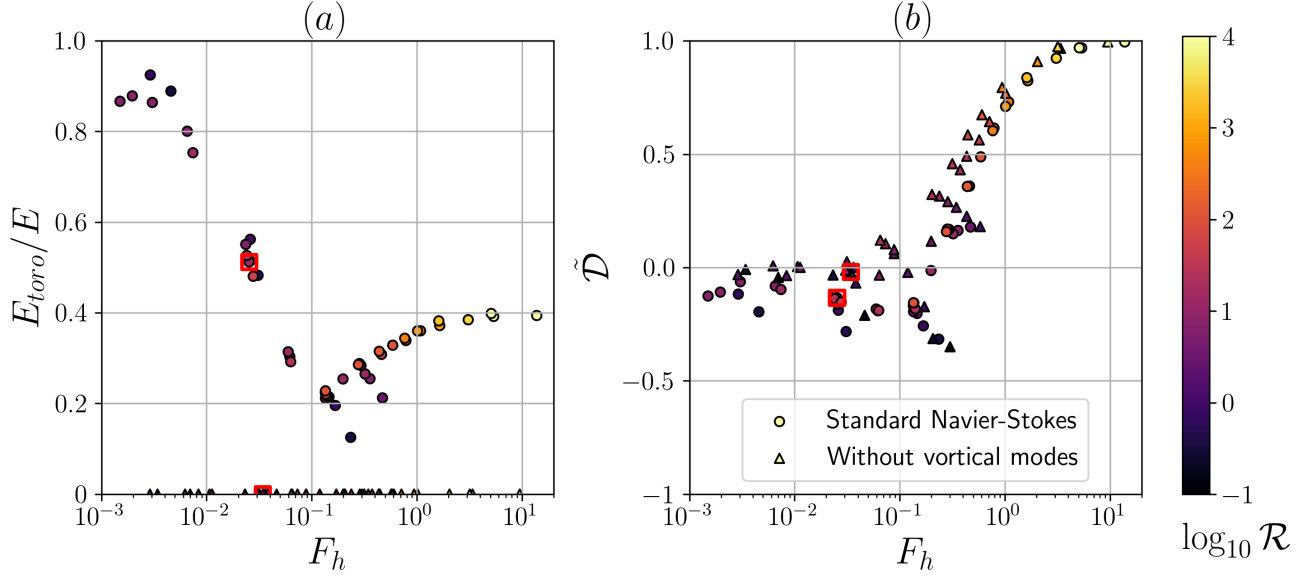


FIG. 3. (a) Ratio of vortical modes energy vs F_h . (b) Relative difference between poloidal and potential energies $\tilde{\mathcal{D}} = (E_{\text{polo}} - E_{\text{pot}})/(E_{\text{polo}} + E_{\text{pot}})$ for simulations with or without vortical modes vs F_h . The red boxes indicate the simulations with $(N, \mathcal{R}_i) = (40, 20)$ investigated in the next subsections.

B. Energy budget in the strongly stratified regime

It is expected that the spatial energy budget will depend on the ratio of temporal timescales. In particular the non-linearity parameter used for several physical systems, including stratified and rotating turbulence [19, 64] and MHD [46, 65]

$$\chi_{L,\mathbf{k}} \equiv \frac{\tau_{L,\mathbf{k}}}{\tau_{NL,\mathbf{k}}} = \frac{(\varepsilon_{\text{kin}} k^2)^{1/3}}{N k_h / k} = \frac{k}{k_h} \left(\frac{k}{k_O} \right)^{2/3} = \frac{1}{\sin \theta_{\mathbf{k}}} \left(\frac{k}{k_O} \right)^{2/3}. \quad (20)$$

It represents the ratio between the period of the linear waves $\tau_{L,\mathbf{k}} = 2\pi k / (N k_h)$ and the eddy turnover time $\tau_{NL,\mathbf{k}} = 2\pi / (k^2 \varepsilon_{\text{kin}})^{1/3}$, estimated by dimensional analysis. In a similar way, we introduce the wave dissipation parameter

$$\chi_{d,\mathbf{k}} \equiv \frac{\tau_{L,\mathbf{k}}}{\tau_{\nu}} = \frac{\nu k^2}{N k_h / k} = \frac{k}{k_h} \left(\frac{k}{k_d} \right)^2 = \frac{1}{\sin \theta_{\mathbf{k}}} \left(\frac{k}{k_d} \right)^2 \quad (21)$$

which represents the ratio between the period of the linear waves $\tau_{L,\mathbf{k}} = 2\pi k / (N k_h)$ and the dissipation time $\tau_{\nu} = 2\pi / (\nu k^2)$. In the last equation, we introduced the wave dissipation wave-vector $k_d \equiv \sqrt{N/\nu}$.

The kinetic energy and potential energy budgets for one Fourier mode read

$$\left\langle \frac{1}{2} \frac{d|\hat{\mathbf{v}}_{\mathbf{k}}|^2}{dt} \right\rangle = \mathcal{I}_{\mathbf{k}} + \mathcal{T}_{\text{kin},\mathbf{k}} - \mathcal{B}_{\mathbf{k}} - \varepsilon_{\text{kin},\mathbf{k}}, \quad \text{and} \quad \left\langle \frac{1}{2N^2} \frac{d|\hat{b}|^2}{dt} \right\rangle = \mathcal{T}_{\text{pot},\mathbf{k}} + \mathcal{B}_{\mathbf{k}} - \varepsilon_{\text{pot},\mathbf{k}}, \quad (22)$$

where

$$\begin{aligned} \mathcal{I}_{\mathbf{k}} &= \left\langle \text{Re} \left(\hat{\mathbf{f}}_{\mathbf{k}} \cdot \hat{\mathbf{v}}_{\mathbf{k}}^* \right) \right\rangle, & \mathcal{T}_{\text{kin},\mathbf{k}} &= - \left\langle \text{Re} \left(\hat{\mathbf{v}}_{\mathbf{k}}^* \cdot \left[\bar{\mathbf{P}}_{\mathbf{k}} \cdot (\widehat{\mathbf{v} \cdot \nabla \mathbf{v}})_{\mathbf{k}} \right] \right) \right\rangle, \\ \mathcal{T}_{\text{pot},\mathbf{k}} &= - \left\langle \text{Re} \left(\hat{b}_{\mathbf{k}}^* (\widehat{\mathbf{v} \cdot \nabla b})_{\mathbf{k}} \right) / N^2 \right\rangle, & \mathcal{B}_{\mathbf{k}} &= - \left\langle \text{Re} \left(\hat{v}_{z\mathbf{k}}^* \hat{b}_{\mathbf{k}} \right) \right\rangle, \\ \varepsilon_{\text{kin},\mathbf{k}} &= (\nu k^2 + \nu_4 k^4) \frac{|\hat{\mathbf{v}}_{\mathbf{k}}|^2}{2}, & \varepsilon_{\text{pot},\mathbf{k}} &= (\kappa k^2 + \kappa_4 k^4) \frac{|\hat{b}_{\mathbf{k}}|^2}{2N^2}, \end{aligned} \quad (23)$$

are respectively the kinetic energy injection rate, the kinetic energy transfer, the potential energy transfer, the conversion of kinetic energy to potential energy, the kinetic energy dissipation, and the potential energy dissipation. In the last equations, $(\cdot)^*$ denotes the complex conjugate, $Re(\cdot)$ the real part, $\langle \cdot \rangle$ stands for the averaging operator, and $\tilde{P}_{\mathbf{k}} = \mathbb{I} - \mathbf{e}_{\mathbf{k}} \otimes \mathbf{e}_{\mathbf{k}}$ is the projector onto the plane orthogonal to \mathbf{k} . In this section, we study azimuthal average of the energy budget. Namely, we computed quantities like:

$$F(k_h, k_z) = \frac{1}{\delta k_h \delta k_z} \sum_{\substack{k_h \leq k'_h < k_h + \delta k_h \\ k_z \leq |k'_z| < k_z + \delta k_z}} F_{\mathbf{k}'}, \quad (24)$$

where F can be E_{pot} , E_{polo} , E_{toro} , $E_{\text{kin}} = E_{\text{polo}} + E_{\text{toro}}$, \mathcal{T}_{pot} , \mathcal{T}_{kin} , \mathcal{B} , \mathcal{I} , ε_{kin} , or ε_{pot} .

Following [19], we use the ratios of energies, like

$$\frac{E_{\text{toro}}(k_h, k_z)}{E(k_h, k_z)} \quad \text{and} \quad \tilde{\mathcal{D}}(k_h, k_z) = \frac{E_{\text{polo}}(k_h, k_z) - E_{\text{pot}}(k_h, k_z)}{E_{\text{polo}}(k_h, k_z) + E_{\text{pot}}(k_h, k_z)}, \quad (25)$$

in order to quantify the energy content scale by scale. In the same spirit, we also introduce for each

$$\tilde{\mathcal{T}}_{\text{kin}}(k_h, k_z) = \frac{\mathcal{T}_{\text{kin}}(k_h, k_z)}{\mathcal{T}_{\text{tot}}(k_h, k_z)}, \quad \tilde{\mathcal{T}}_{\text{pot}}(k_h, k_z) = \frac{\mathcal{T}_{\text{pot}}(k_h, k_z)}{\mathcal{T}_{\text{tot}}(k_h, k_z)}, \quad \tilde{\mathcal{B}}(k_h, k_z) = \frac{\mathcal{B}(k_h, k_z)}{\mathcal{T}_{\text{tot}}(k_h, k_z)}, \quad (26)$$

where

$$\mathcal{T}_{\text{tot}}(k_h, k_z) \equiv |\mathcal{T}_{\text{kin}}(k_h, k_z)| + |\mathcal{T}_{\text{pot}}(k_h, k_z)| + |\mathcal{B}(k_h, k_z)| + \varepsilon_{\text{kin}}(k_h, k_z) + \varepsilon_{\text{pot}}(k_h, k_z). \quad (27)$$

These quantities are useful for tracking the energy pathways scale by scale. By construction, $\tilde{\mathcal{T}}_{\text{pot}}$, $\tilde{\mathcal{T}}_{\text{kin}}$, and $\tilde{\mathcal{B}}$ vary between -1 and 1 depending on the amplitude and direction of the energy transfer or conversion ($\tilde{\mathcal{B}} > 0$ corresponds to conversion of kinetic energy to potential energy). In statistically stationary state ($\langle \dot{\cdot} \rangle = 0$) and in the inertial range ($\varepsilon_{\text{kin}}(k_h, k_z) \simeq 0$, $\varepsilon_{\text{pot}}(k_h, k_z) \simeq 0$, $\mathcal{I}(k_h, k_z) = 0$), we should have $\mathcal{T}_{\text{kin}}(k_h, k_z) \simeq -\mathcal{T}_{\text{pot}}(k_h, k_z) \simeq \mathcal{B}(k_h, k_z)$. For this reason, we will present only $\tilde{\mathcal{B}}(k_h, k_z)$.

1. Energy spectra

Figure 4 shows the 1D spatial spectra, and the normalized (divided by the total energy dissipation ε) energy fluxes along k_h for simulations with $(N, \mathcal{R}_i) = (40, 20)$. We first observe that removing vortical modes does not change the behavior of the poloidal and potential energy spectra (Figure 4(a)-(b)): the horizontal spectra are close to $k_h^{-5/3}$, with a bottleneck beyond the buoyancy wave-vector, while the vertical spectra has a spectral slope between -2 and -3 . The kinetic energy flux $\Pi_{\text{kin}}(k_h)$ and the potential energy flux $\Pi_{\text{pot}}(k_h)$ start to show a plateau over almost a decade in these simulations (Figure 4(c)-(d)). We observe that the dissipation starts to be important at the Ozmidov scale, meaning that this simulations lies between the strongly stratified turbulence regime and the viscosity affected regime [29]. The main effect of removing vortical modes is to make $\Pi_{\text{pot}}(k_h)$ larger than $\Pi_{\text{kin}}(k_h)$. Also, the kinetic energy dissipation $\varepsilon_{\text{kin}}(k_h)$ is almost equal to the potential energy dissipation $\Pi_{\text{pot}}(k_h)$ when vortical modes are removed, as we expect for a system of internal gravity waves [45].

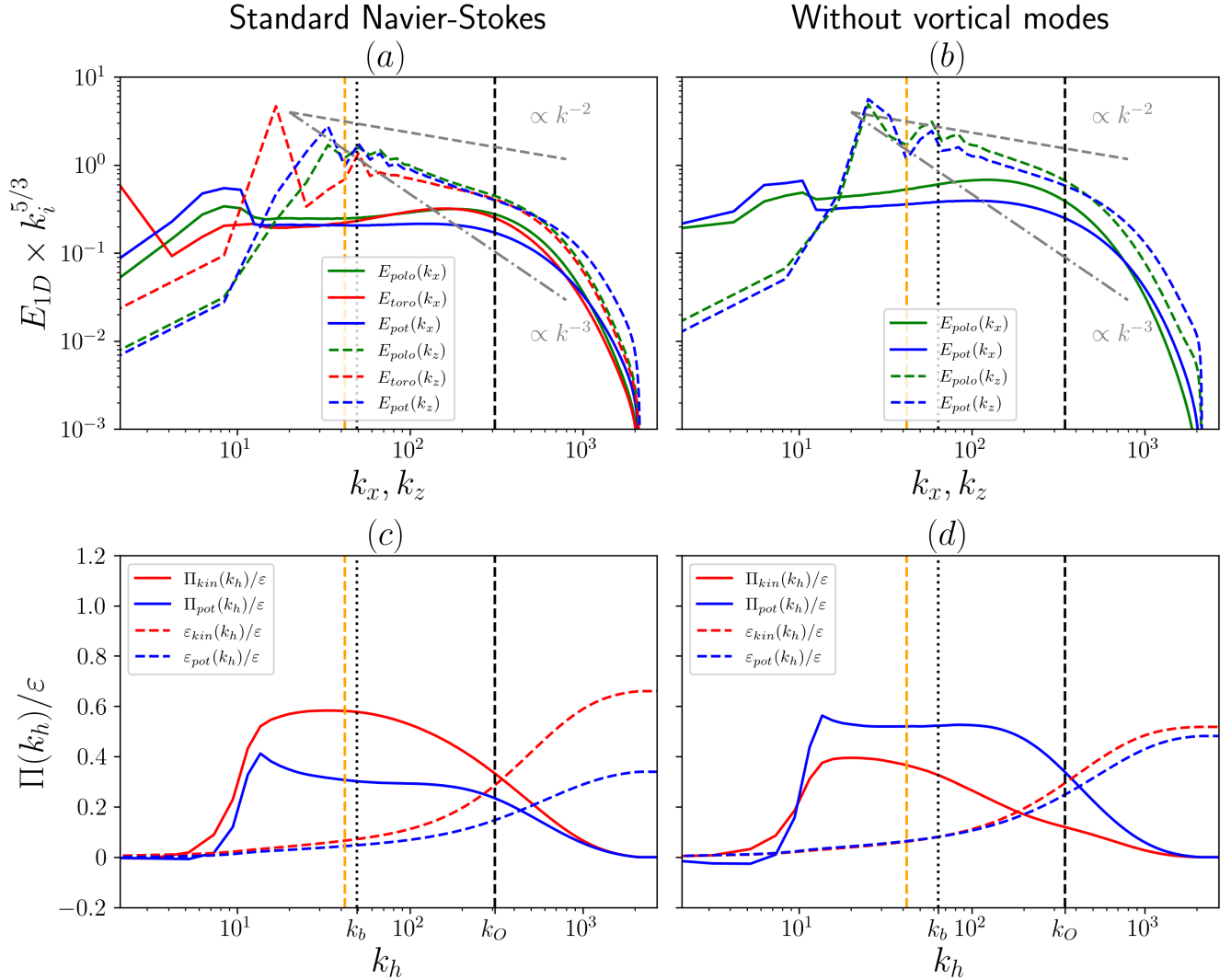


FIG. 4. Compensated 1D spatial energy spectra for simulations $(N, \mathcal{R}_i) = (40, 20)$ with (a) and without (b) vortical modes. Normalized k_h energy fluxes for the same simulations with (c) and without (d) vortical modes. The orange dotted line corresponds to the maximal wave-vector modulus of the forcing region, the black dotted line to k_b , the black dashed line to k_O .

Figure 5 shows slices of the kinetic energy spectra for the same simulations. The potential and kinetic energy spectra have the same trends with respect to k_h and k_z , so the potential energy spectra is not presented. As in [19], we observe different scaling laws depending on the region in the (k_h, k_z) plane. Namely, important differences between small k_z and large k_z for a given k_h (panels (a) and (b) on figure 5):

- For $k_h \ll k_b$, energy is accumulated at the lowest available k_h and small k_z , as usual in stratified turbulence [59, 60, 66]. At $k_z \ll k_b$ the spectra is close to a k_h^{-2} dependency, which is consistent with integrated energy spectra reported in earlier studies [30, 31], but not with the WWT predictions (4). This also indicates a transfer of energy to large scale, already investigated in [59, 66]. For a fixed $k_z \gg k_b$, we rather observe $E_{\text{kin}} \sim k_h^1$ which would correspond to an equipartition of energy in horizontal scales.
- For $k_h \gg k_b$, the spectra starts to depend less and less on k_z , and the $E_{\text{kin}}(k_h, k_z)$ slices eventually merge around $k_h \sim k_O$, when the eddy turnover time starts to be less than the period of any linear waves, i.e. $\chi_{L, \mathbf{k}} > 1$.

Important differences can also be noted when looking at k_z slices (panels (c) and (d) on figure 5):

- For $k_z \ll k_b$, the spectra is close to $\sim k_z^0$, indicating that horizontal layers of height larger than the buoyancy scale are decoupled in these strongly stratified simulations.

- For $k_b \ll k_z \ll k_O$, the spectra is very steep at small horizontal wave-vectors, while it remains flat at large horizontal wave-vectors.
- For $k_z \gg k_O$, the spectral slope starts to depend less and less on k_h . Yet, the $E_{\text{kin}}(k_h, k_z)$ does not merge around $k_h \sim k_O$ since small horizontal scales are more energetic compared to the large horizontal scales.

Due to the reduced aspect ratio of our simulations, we do not observe a net separation between the forcing and the buoyancy scales. Still, the spectra remains very similar to the one presented in [19]. Interestingly, the trends of the kinetic energy spectra appear to be very similar, whatever vortical modes are present or not. This is a first indication that the presence of vortical modes is not the only obstacle to observe internal gravity wave turbulence in realistic flows.

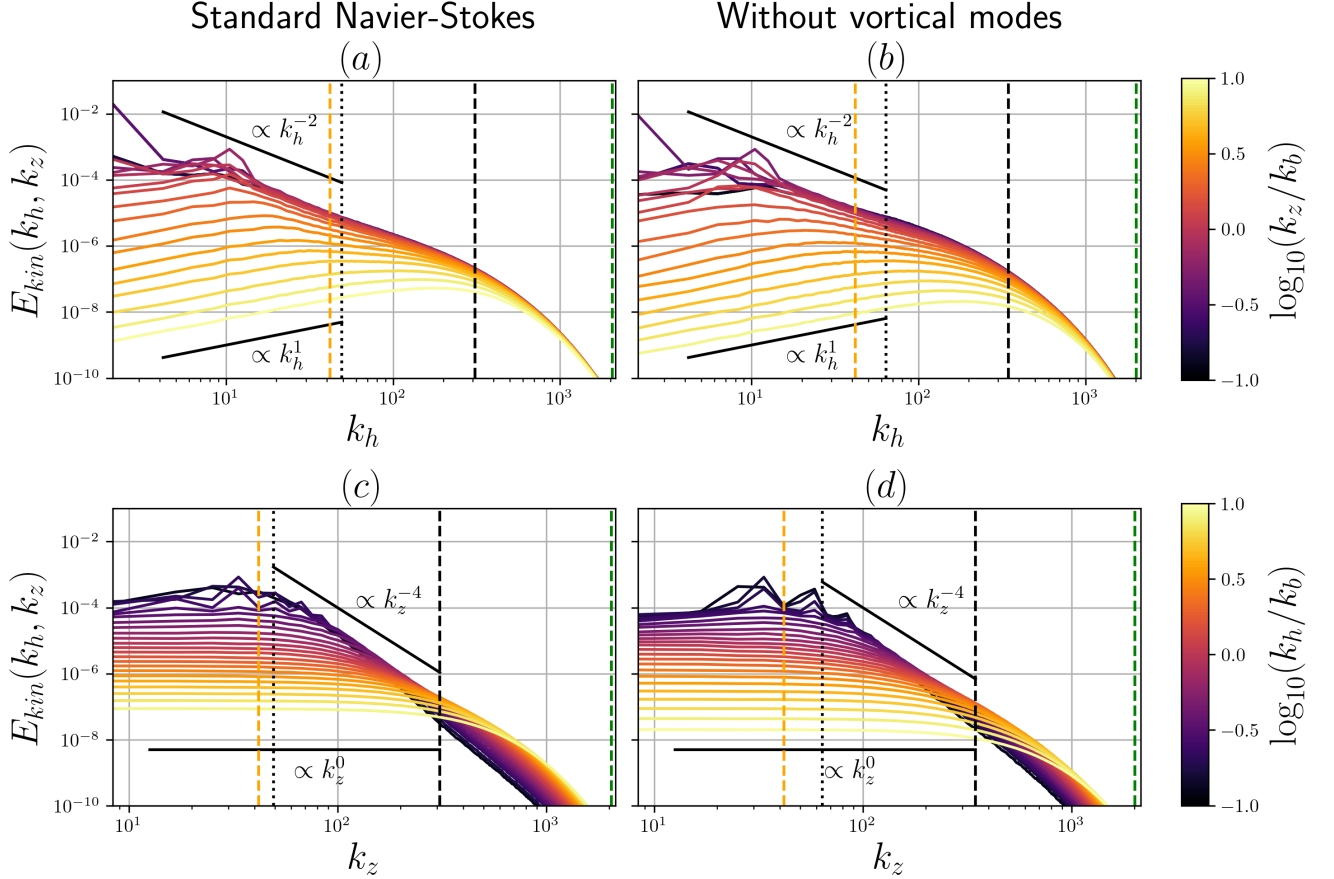


FIG. 5. Slices of the kinetic energy spectra $E_{\text{kin}}(k_h, k_z)$ for simulations $(N, \mathcal{R}_i) = (40, 20)$ with and without vortical modes. The orange dotted line corresponds to the maximal wave-vector modulus of the forcing region, the black dotted line to k_b , the black dashed line to k_O , and the green dashed line to the dissipative wave-vector. (a) E_{kin} vs k_h with vortical modes. (b) E_{kin} vs k_h without vortical modes. (c) E_{kin} vs k_z with vortical modes. (d) E_{kin} vs k_z without vortical modes.

Figure 6 shows the k_h - k_z spectra. Obviously, the simulation without vortical modes has no energy in the toroidal velocity. We observe that the energy is contained at large scales. When vortical modes are present, an important part of the energy is contained in one vortical mode $(k_h, k_z) = (\delta k_h, 3\delta k_z)$, corresponding to large, vertically stacked vortex with varying orientations (Figure 6(a)). When vortical modes are removed, energy is still concentrated in the same wave-vectors, but under the form of poloidal and potential energy (Figure 6(d)-(f)). Except this qualitative difference, we observe that toroidal, poloidal, and potential energy spectra show the same trends.

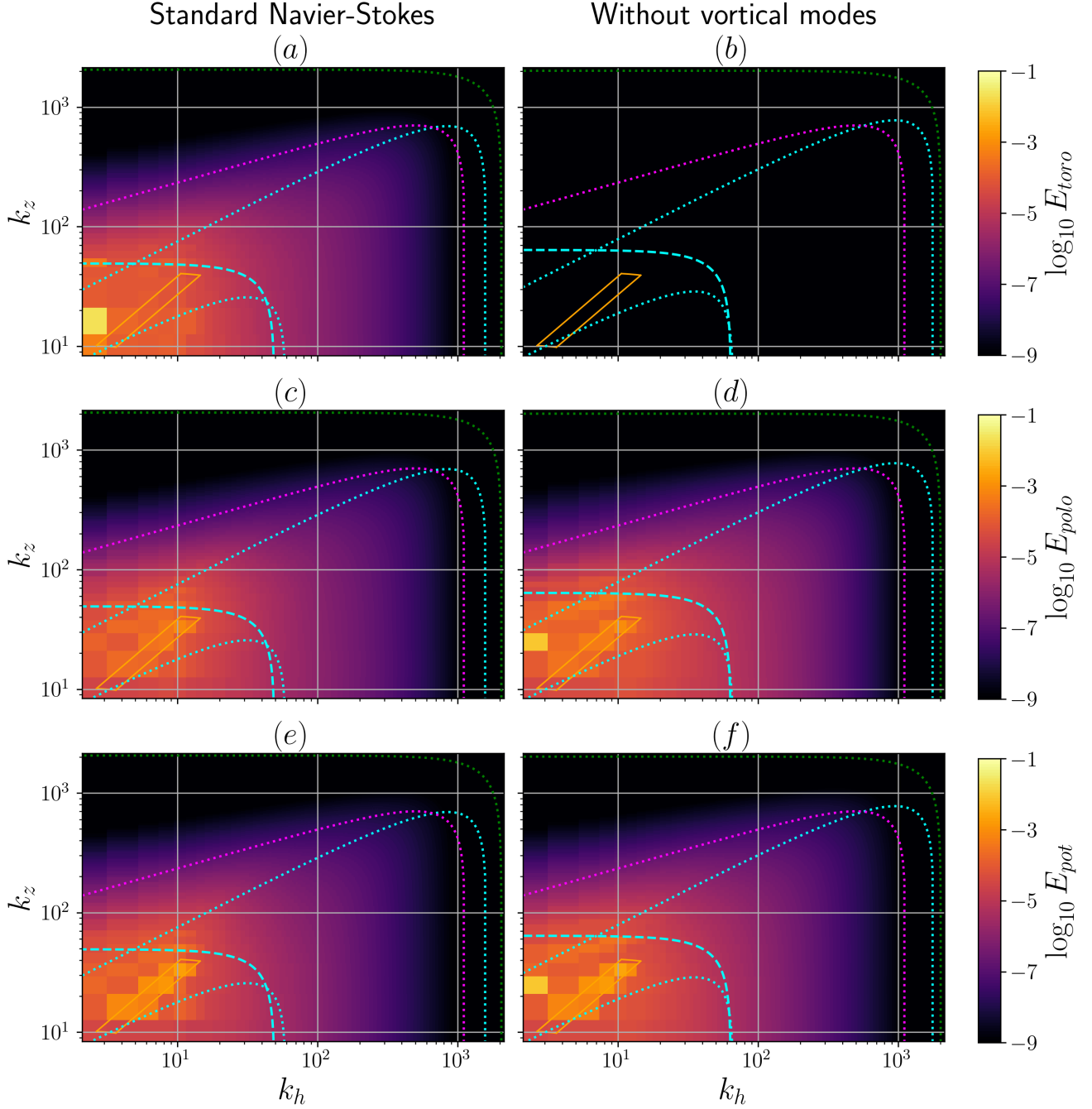


FIG. 6. k_h - k_z spectra for the simulations at $(N, \mathcal{R}_i) = (40, 20)$, with and without vortical modes. The cyan dotted lines correspond to $\chi_{L,\mathbf{k}} = 1/3$ and $\chi_{L,\mathbf{k}} = 3$, the cyan dashed line to $k = k_b$, the magenta dotted line to $\chi_{d,\mathbf{k}} = 1$, and the green dotted line to the dissipative scale. The orange box corresponds to the forcing region. (a) E_{toro} with vortical modes. (b) E_{toro} without vortical modes. (c) E_{polo} with vortical modes. (d) E_{polo} without vortical modes. (e) E_{pot} with vortical modes. (f) E_{pot} without vortical modes.

In order to have a finer analysis of the distribution of energy in the k_h - k_z plane, it is useful to look at energy ratios shown on Figure 7. One clearly observes that E_{toro} is never negligible away of the forcing region, and very important for small wave-vectors when the vortical modes are not removed (Figure 7(a)-(b)). Except this important difference, the spectral energy budgets of the two simulations appear to share striking similarities for these simulations with $F_h \ll 1$ and $\mathcal{R} \gg 1$. Outside the forcing region, the poloidal energy is dominant ($\tilde{D} > 0$) between the lines $\chi_{L,\mathbf{k}} = 1/3$ and $\chi_{L,\mathbf{k}} = 3$, corresponding to a region where the critical balance condition $\chi_{L,\mathbf{k}} \sim 1$ is fulfilled (Figure 7(c)-(d)).

The potential energy is dominant ($\tilde{\mathcal{D}} < 0$) when $\chi_{L,\mathbf{k}} > 3$, i.e. in a region where eddies are faster than waves. We observe a good equipartition between potential and poloidal energy ($\tilde{\mathcal{D}} \simeq 0$) when $\chi_{L,\mathbf{k}} < 1/3$, i.e. in the region where waves are faster than eddies. This indicates that the ratio of temporal scales $\chi_{L,\mathbf{k}}$ is important when identifying ranges in anisotropic turbulence, as already explained in [19]. In particular, it shows that a wave dominated range cannot lie above $\chi_{L,\mathbf{k}} > 1/3$, which is marked by wave-breaking and strong vortices.

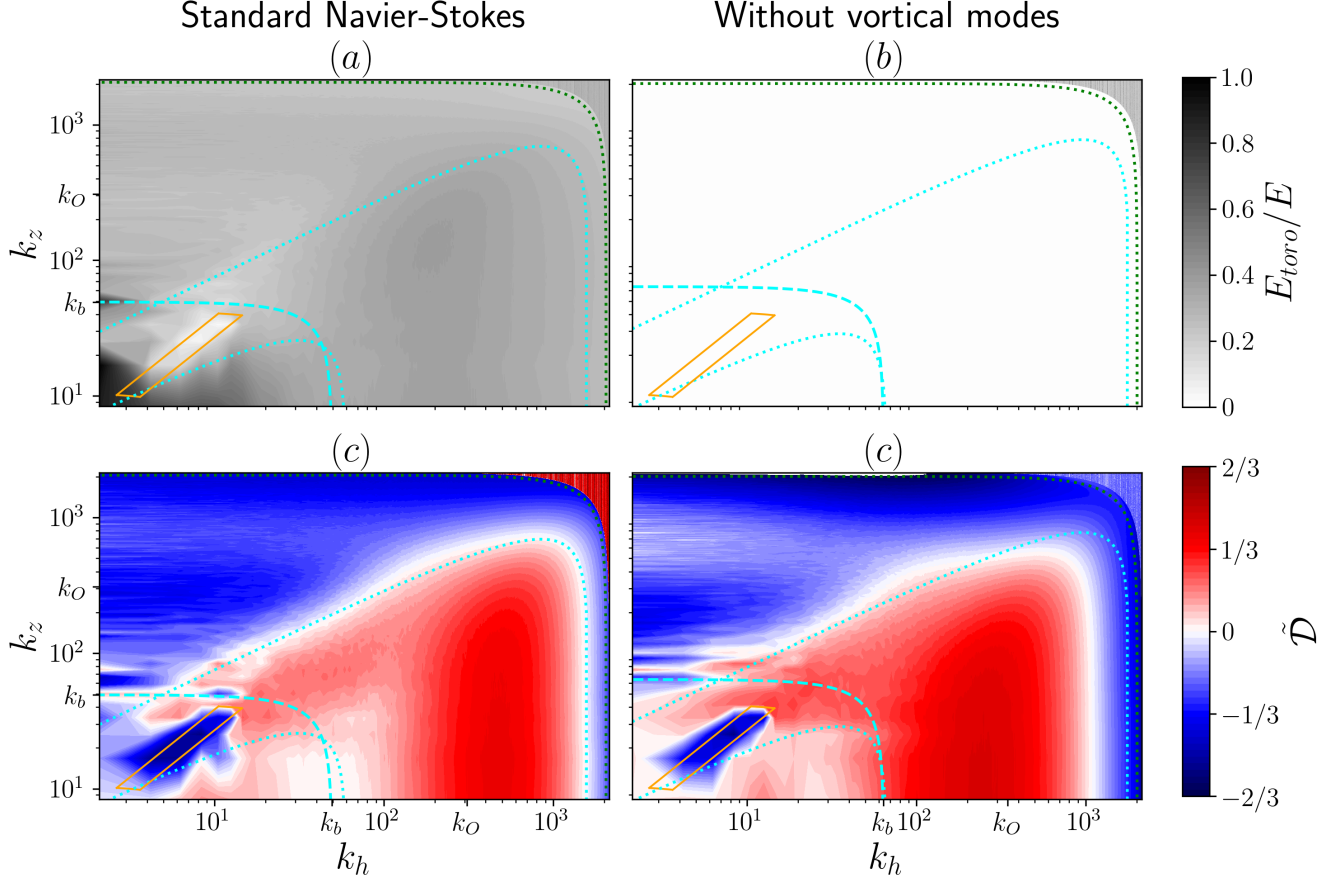


FIG. 7. Ratios of energy for the simulations at $(N, \mathcal{R}_i) = (40, 20)$, with and without vortical modes. The cyan dotted lines correspond to $\chi_{L,\mathbf{k}} = 1/3$ and $\chi_{L,\mathbf{k}} = 3$, the cyan dashed line to $k = k_b$, the green dotted line to the dissipative scale, and the continuous black line to $k_z = k_h$. The orange box corresponds to the forcing region. (a) E_{toro}/E with vortical modes. (b) E_{toro}/E without vortical modes. (c) $\tilde{\mathcal{D}} = (E_{\text{polo}} - E_{\text{pot}})/(E_{\text{polo}} + E_{\text{pot}})$ with vortical modes. (d) $\tilde{\mathcal{D}}$ without vortical modes.

2. Conversion of kinetic to potential energy

We can observe on Figure 8 that the conversion between potential energy and kinetic energy $\tilde{\mathcal{B}}$ are also very similar with or without vortical modes. This is not surprising since the vertical velocity is fully contained in waves modes, and not in vortical modes. Naturally, the amplitude of $\tilde{\mathcal{B}}$ is important only when $\chi_{d,\mathbf{k}} < 1$, meaning that waves need to not be damped too strongly by viscosity in order to convert potential energy to kinetic energy (or conversely). Yet, we observe that $\tilde{\mathcal{B}}$ is whether positive or negative in average, even in the region $\chi_{L,\mathbf{k}} < 1/3$. Consequently, if waves certainly exist in this range, they cannot subsist because their kinetic energy is converted into potential energy or vice-versa. Therefore, these simulations are unlikely to correspond to a WWT regime, even in the buoyancy range and without vortical modes. Nevertheless, we observe that $\tilde{\mathcal{B}}$ fluctuates in time in the buoyancy range ($k \leq k_b$).

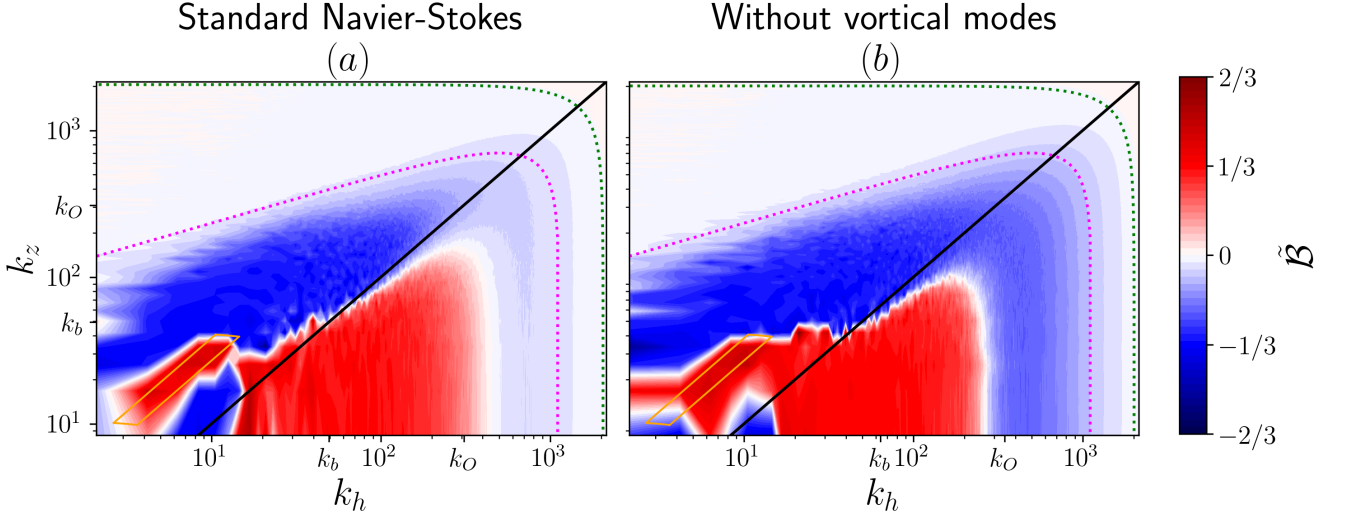


FIG. 8. Normalized conversion to potential energy for the simulations at $(N, \mathcal{R}_i) = (40, 20)$, with (a) and without (b) vortical modes. The magenta dotted line corresponds to $\chi_{d,k} = 1$, the green dotted line to the dissipative scale, and the continuous black line to $k_z = k_h$. The orange box corresponds to the forcing region.

C. Spatiotemporal analysis in the buoyancy range

From the previous subsection, it is expected that waves can dominate (but cannot necessarily sustain) not too far from the buoyancy range ($k \leq k_b$). To assess further the presence and degree of non-linearity of waves, we performed a spatiotemporal analysis for small k . As explained in the previous subsection, waves are marked by an equipartition between poloidal kinetic energy and potential energy. This motivates us to introduce the equipartition energy and the difference energy as

$$E_{\text{equi}}(k_h, k_z) = 2 \min \{ E_{\text{polo}}(k_h, k_z), E_{\text{pot}}(k_h, k_z) \}, \quad (28)$$

$$E_{\text{diff}}(k_h, k_z) = E_{\text{polo}}(k_h, k_z) + E_{\text{pot}}(k_h, k_z) - E_{\text{equi}}(k_h, k_z), \quad (29)$$

in order to track the presence of waves in the (k_h, k_z) plane. Indeed, E_{diff} corresponds to the energy contained in E_{pot} and E_{polo} that cannot be in potential-kinetic equipartition. Therefore, E_{diff} does not contain the waves' energy. On the other side, E_{equi} corresponds to the energy contained in E_{pot} and E_{polo} that is in potential-kinetic equipartition. Consequently, E_{equi} encompass the waves' energy. However, it is important to note that E_{equi} can also contain the energy of structures that are not waves. A more careful separation between waves and non-waves structures requires a 4D spatiotemporal filtering [40, 41], which is expansive in term of computational time and data storage. Yet, E_{equi}/E and E_{diff}/E help to track waves in the (k_h, k_z) plane at a lower cost.

Figure 9 shows slices of $E_{\text{equi}}(k_h, k_z, \omega)$ at large spatial scales, namely $k_h = 25.1$ and $k_z = 25.1$. We observe that the energy tends to be concentrated around the linear wave frequency only at large spatial scales, but is dispersed even in the simulations without vortical modes. It has been shown that this dispersion could be quantified by considering a Doppler effect due to the advection of internal waves by shear modes [39]. Despite the fact that shear modes are removed in our simulations, we can try to give such a prediction by considering that a Doppler shift is due to a horizontal mean flow \mathbf{U} of amplitude U_h

$$\delta\omega_{\text{doppler}} = \max_{\varphi_{\mathbf{k}}} \mathbf{U} \cdot \mathbf{k} = kU_h \sin \theta_{\mathbf{k}} = \frac{k}{k_b} \omega_{\mathbf{k}}. \quad (30)$$

This gives a reasonable explanation of the important dispersion.

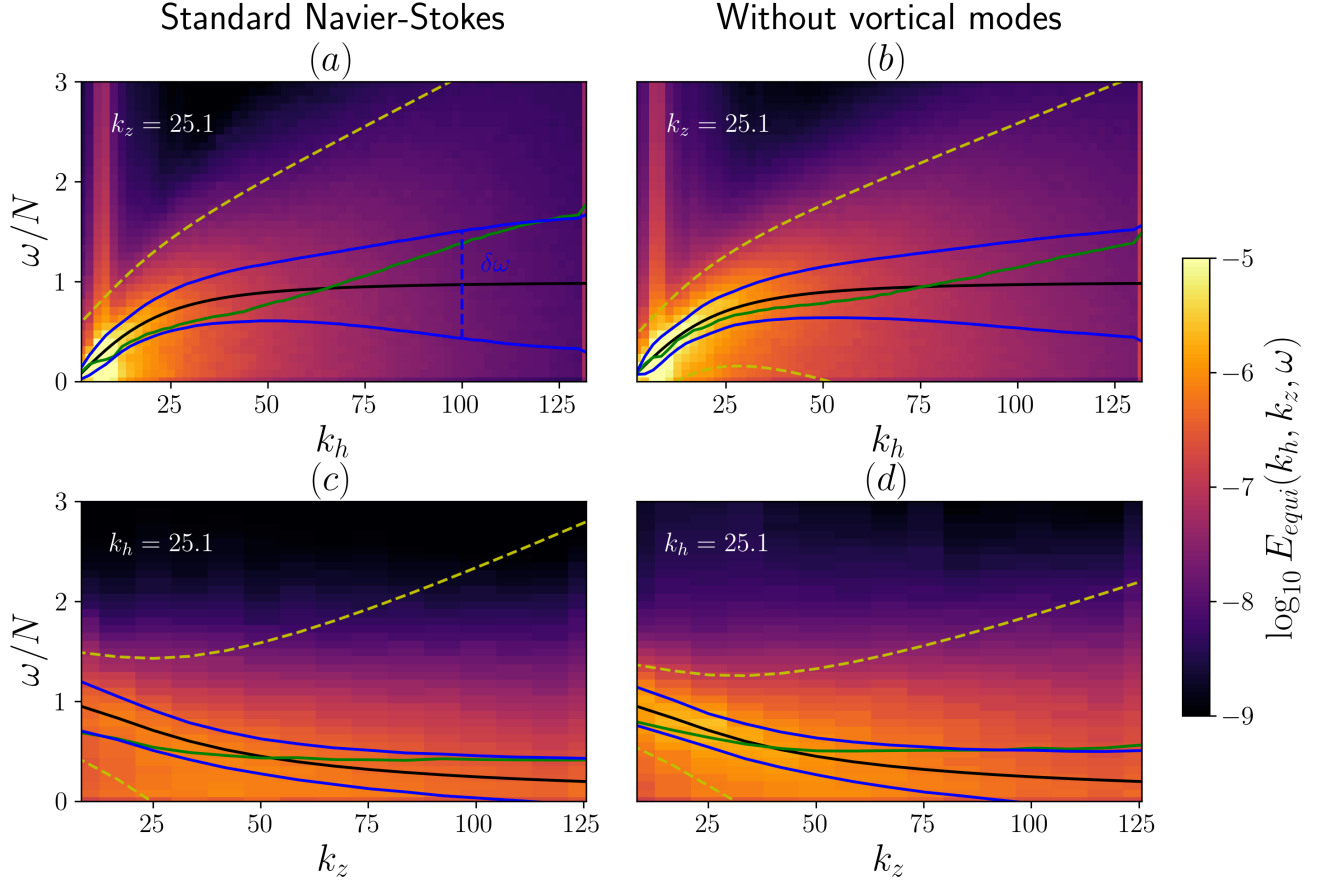


FIG. 9. Slices of $E_{\text{equi}}(k_h, k_z, \omega)$ for the simulations at $(N, \mathcal{R}_i) = (40, 20)$, with and without vortical modes. (a) $k_z = 25.1$ with vortical modes. (b) $k_z = 25.1$ without vortical modes. (c) $k_h = 25.1$ with vortical modes. (d) $k_h = 25.1$ without vortical modes. The linear dispersion relation $\omega_{\mathbf{k}} = Nk_h/k$ is plotted in black, the empirical frequency ω_{emp} in green, the lines $\omega_{\mathbf{k}} \pm \delta\omega/2$ in blue, and the yellow dashed lines corresponds to the lines $\omega_{\mathbf{k}} \pm \delta\omega_{\text{doppler}}$ (30).

To observe more precisely the dispersion in spatiotemporal scales, we represent the ratio $E_{\text{equi}}(k_h, k_z, \omega) / \max_{\omega} E(k_h, k_z, \omega)$ on Figure 10, which indicates how the energy is distributed among temporal scales for a given spatial scale. For a system of weakly nonlinear internal gravity waves, we should observe a pic of E_{equi}/E around $\omega = \omega_{\mathbf{k}}$ (for the energy to be concentrated around the linear frequency), whose maxima should be close to unity (for the energy to be concentrated in waves modes). For these simulations, we observe that the concentration of energy around the linear frequency mostly depends on the ratio k/k_b . As expected, the pics of energy around $\omega = \omega_{\mathbf{k}}$ is more pronounced when $k \ll k_b$. This is an indication that linear waves effectively dominate only if $k \ll k_b$, with or without vortical modes. When $k \simeq k_b$, energy starts to spread at all temporal scales. We note that removing vortical modes from the dynamics helps to concentrate E_{equi} in temporal scales since temporal spectra tend to be more picked at intermediate k/k_b . For more, simulations without vortical modes naturally have bigger E_{equi}/E at all spatial and temporal scales (Figure 10(d)) when compared to simulations with vortical modes (Figure 10(c)).

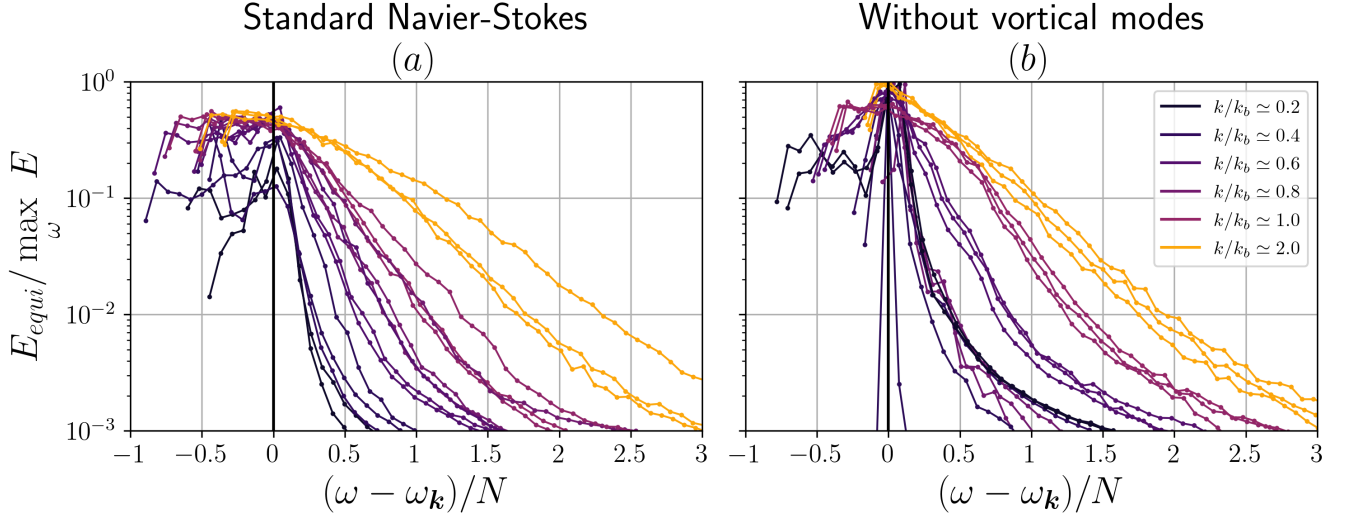


FIG. 10. Spatiotemporal analysis of the simulations with $(N, \mathcal{R}_i) = (40, 20)$. $E_{\text{equi}}(k_h, k_z, \omega)/E(k_h, k_z, \omega)$ for the simulation with vortical modes (a) and for the simulation without vortical modes (b). Only some couples (k_h, k_z) are shown. Lines' colors corresponds to different values of k/k_b . The vertical black lines corresponds to $\omega = \omega_{\mathbf{k}}$.

A way to measure the distribution of energy in temporal scales is to compute the empirical frequency ω_{emp} and the deviation from linear waves frequency $\delta\omega$, computed with the waves energy spectra. Here, we estimate them using the equipartition energy spectra such that

$$\omega_{\text{emp}}(k_h, k_z) = \frac{\sum_{\omega} \omega E_{\text{equi}}(k_h, k_z, \omega)}{\sum_{\omega} E_{\text{equi}}(k_h, k_z, \omega)} \quad \text{and} \quad \delta\omega(k_h, k_z) = \sqrt{\frac{\sum_{\omega} (\omega - \omega_{\mathbf{k}})^2 E_{\text{equi}}(k_h, k_z, \omega)}{\sum_{\omega} E_{\text{equi}}(k_h, k_z, \omega)}}. \quad (31)$$

The quantity $\delta\omega/\omega_{\mathbf{k}}$ is another estimation of the strength non linear interactions. Contrary to the non-linearity parameter $\chi_{L, \mathbf{k}}$, which is derived by dimensional analysis, $\delta\omega/\omega_{\mathbf{k}}$ requires the knowledge of the spatio-temporal spectra. $\delta\omega/\omega_{\mathbf{k}}$ is called non-linear broadening, and is particularly important in the the WWT theory: for $\delta\omega/\omega_{\mathbf{k}} \gg 1$, waves' dynamics is strongly affected by non-linear interactions, while when $\delta\omega/\omega_{\mathbf{k}} \ll 1$, waves can propagate with only weak non-linear perturbations and the theory could hold [2]. For a system of non-interacting linear waves, both $|\omega_{\text{emp}} - \omega_{\mathbf{k}}|/N$ and $\delta\omega/\omega_{\mathbf{k}}$ should be zero. Figure 11 shows this quantities in the (k_h, k_z) plane. It shows that the empirical frequency is close to $\omega_{\mathbf{k}}$, and that the nonlinear broadening is small if $k \ll k_b$ and $\chi_{L, \mathbf{k}} \leq 1/3$, which is consistent with previous results [19]. Conversely, ω_{emp} deviates significantly from $\omega_{\mathbf{k}}$ and $\delta\omega/\omega_{\mathbf{k}}$ becomes large when $k \gg k_b$ or $\chi_{L, \mathbf{k}} > 3$. We observed that removing vortical modes does not have a significant direct effect on ω_{emp} and $\delta\omega/\omega_{\mathbf{k}}$. However, the simulations without vortical modes tend to have smaller F_h , which increases the size of the buoyancy range when compared to the simulations with vortical modes.

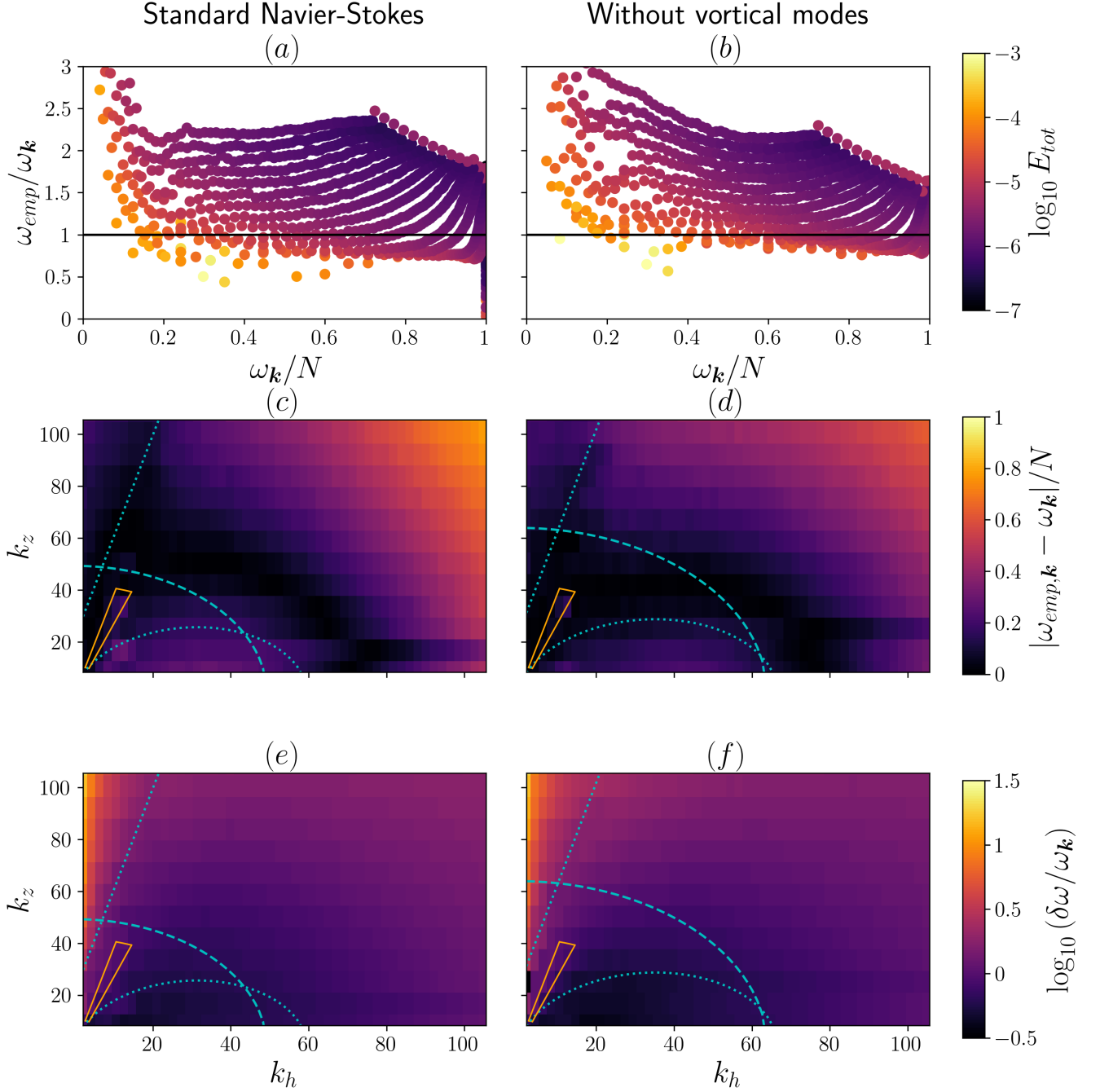


FIG. 11. $\omega_{emp}/\omega_{\mathbf{k}}$ vs $\omega_{\mathbf{k}}/N$ for simulations with $(N, \mathcal{R}_i) = (40, 20)$, with vortical modes (a) and without vortical modes (b). $|\omega_{emp} - \omega_{\mathbf{k}}|/N$ for simulation with vortical modes (c) and without vortical modes (d). $\delta\omega/\omega_{\mathbf{k}}$ for simulation with vortical modes (e) and without vortical modes (f). Dotted lines correspond to $\chi_{L, \mathbf{k}} = 1/3$ and $\chi_{L, \mathbf{k}} = 3$, the dashed line to $k = k_b$, and the orange box to the forcing region.

D. Waves energy in the parameters space

The previous subsections aimed to present the dispersion in temporal scales for one couple of simulations, but we did not quantify the amount of waves in the (k_h, k_z) plane, nor in the (F_h, \mathcal{R}) so far. This is the goal of this subsection. In order to quantify waves' energy in a flow, we propose to simply filter the spatiotemporal spectra E_{equi} by a Gaussian weight with mean $\omega_{\mathbf{k}}$ and rms $\epsilon\omega_{\mathbf{k}}$, where ϵ is an arbitrary but small parameter, such that the waves'

energy at a given (k_h, k_z, ω) is

$$E_{\text{wave}}(k_h, k_z, \omega) = E_{\text{equi}}(k_h, k_z, \omega) \exp \left[-\frac{1}{2} \left(\frac{\omega - \omega_{\mathbf{k}}(k_h, k_z)}{\epsilon \omega_{\mathbf{k}}(k_h, k_z)} \right)^2 \right]. \quad (32)$$

Slices of the E_{wave} are represented on Figure 12(a)-(b) for $\epsilon = 0.1$. We observed that choosing this value for ϵ gives a sufficiently narrow window to keep only the spatiotemporal region corresponding to internal gravity waves, while keeping the window sufficiently wide in order to avoid binning effects so we kept $\epsilon = 0.1$. This window with variable wide allows to get rid of the energy of non-wave structures present at low frequency [39]. We can first look at the distribution of the wave's energy in the (k_h, k_z) plane. In order to allow a fair comparison between simulations with or without vortical modes, we introduce the wave's energy ratio

$$\tilde{E}_{\text{wave}}(k_h, k_z) = \frac{E_{\text{wave}}(k_h, k_z)}{E_{\text{polo}}(k_h, k_z) + E_{\text{pot}}(k_h, k_z)}. \quad (33)$$

with

$$E_{\text{wave}}(k_h, k_z) = \sum_{\omega} E_{\text{wave}}(k_h, k_z, \omega) \quad (34)$$

Moreover, normalizing the wave's energy by the total energy (i.e. including vortical modes energy) would have mask the presence of waves in the simulation with vortical modes, since they represent an important part of the energy (Figure 7(a)). \tilde{E}_{wave} is depicted on Figure 12(c)-(d). We observe that \tilde{E}_{wave} tends to be higher for simulations without vortical modes, but removing vortical modes does not change the variations of \tilde{E}_{wave} in the (k_h, k_z) plane for these simulations. As we could have expected from previous works [19] and the previous subsections, we observe that \tilde{E}_{wave} is higher in the buoyancy range, in particular where $\chi_{L, \mathbf{k}} \leq 1/3$. Yet, we also observe that \tilde{E}_{wave} tends to be bigger at very specific angles, smaller than the forcing angle θ_f . This accumulation of internal gravity wave's energy at specific propagation angles has been reported in earlier studies (see e.g. [39]). In the present simulations, we can explain this by invoking Triadic Resonance Instabilities (TRI) between internal gravity waves [42], in particular the PSI [52, 55]. Considering that a primary wave of frequency $\omega_f = \omega_0^* = N \sin \theta_f$ is excited by the forcing, and then decay into two daughter waves of frequency ω_1^* according to the PSI mechanism, we can deduce ω_1^* and the associated propagation angle θ_1^* :

$$\omega_1^* = \frac{\omega_0^*}{2} = 0.15 N \quad \Rightarrow \quad \theta_1^* = \arcsin \left(\frac{\omega_1^*}{N} \right) \simeq 0.15. \quad (35)$$

Invoking, for a second time, the PSI mechanism for the waves of frequency ω_1^* , we can deduce another harmonic

$$\omega_2^* = \frac{\omega_1^*}{2} = 0.075 N \quad \Rightarrow \quad \theta_2^* = \arcsin \left(\frac{\omega_2^*}{N} \right) \simeq 0.075. \quad (36)$$

We can deduce a third harmonic by considering that two waves of frequencies ω_1^* and ω_2^* interact to give a third wave with frequency

$$\omega_3^* = \omega_1^* + \omega_2^* = 0.225 N \quad \Rightarrow \quad \theta_3^* = \arcsin \left(\frac{\omega_3^*}{N} \right) \simeq 0.225. \quad (37)$$

θ_0^* , θ_1^* , θ_2^* , and θ_3^* are reported on Figure 12(c)-(d). We see that they collapse well with the high values of \tilde{E}_{wave} observed at small angles. These give evidences that waves at both high and small frequencies are excited in our strongly stratified simulations, and that they can interact by TRI.

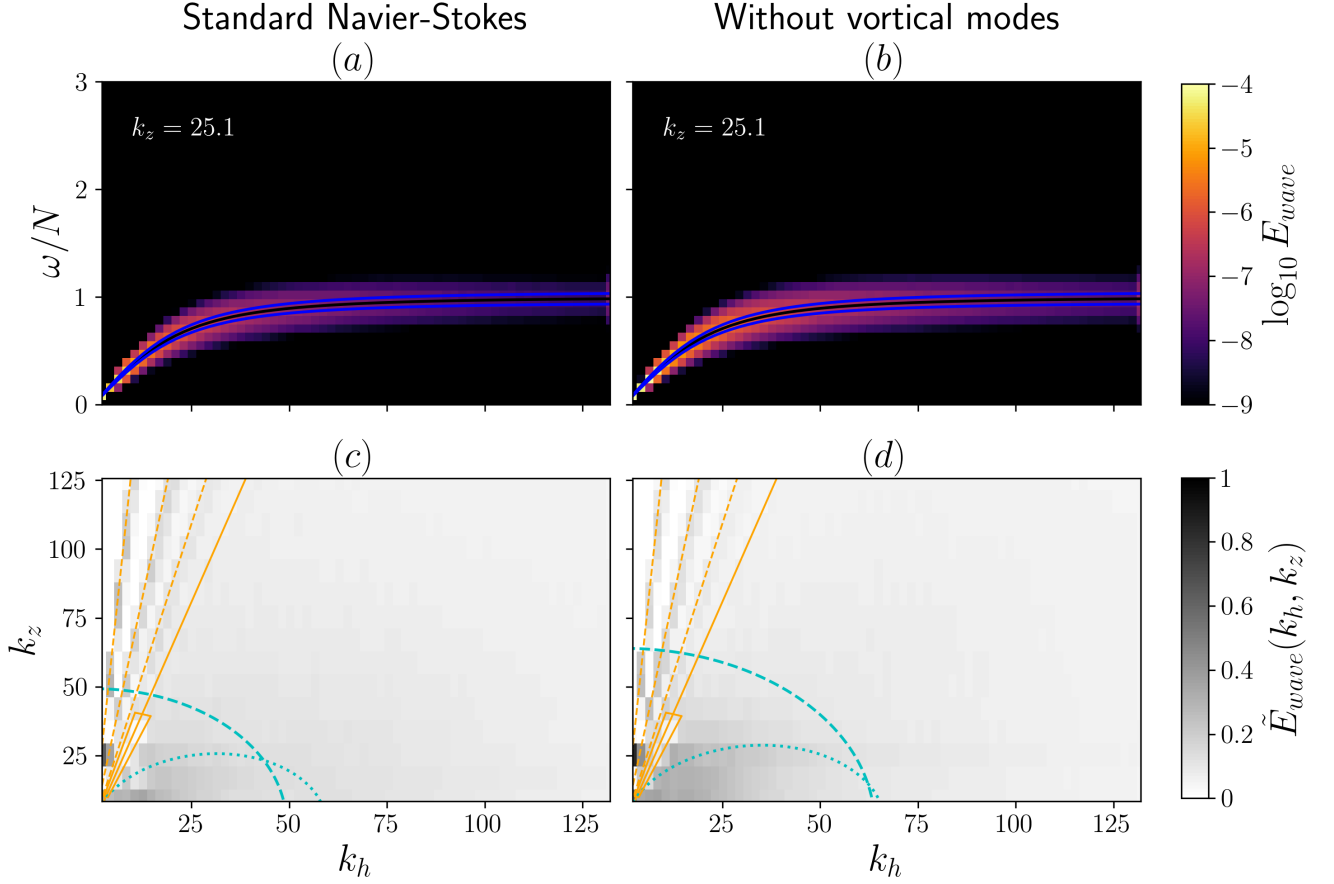


FIG. 12. Slices of the E_{wave} (32) for simulations with $(N, \mathcal{R}_i) = (40, 20)$ and $k_z = 25.1$: with vortical modes (a), and without vortical modes (b). Blue lines correspond to $\omega_{\mathbf{k}} \pm \epsilon\omega_{\mathbf{k}}/2$. $\tilde{E}_{\text{wave}}(k_h, k_z)$ (33) for the same simulations: with vortical modes (c), and without vortical modes (d). The cyan dotted lines correspond to $\chi_{L,\mathbf{k}} = 1/3$, and the cyan dashed line to $k = k_b$. The orange box corresponds to the forcing region. The forcing angle θ_f is represented by a full orange line, while first harmonics (35-37) excited by the TRI are indicated by dashed orange lines.

The spatiotemporal analysis performed in this subsections allows to give a more precise measure of the dominance of waves in the spectral space at a given (F_h, \mathcal{R}) . Now we can use the following quantity

$$\tilde{E}_{\text{wave}} = \frac{\sum_{k_h, k_z, \omega} E_{\text{wave}}(k_h, k_z, \omega)}{\sum_{k_h, k_z} E_{\text{polo}}(k_h, k_z) + E_{\text{pot}}(k_h, k_z)} \quad (38)$$

in order to quantify the dominance of waves for a given simulation, and study its variations in the (F_h, \mathcal{R}) parameters' space, as depicted on Figure 13. Consistently with the previous subsections, we observe that removing vortical modes helps to get higher \tilde{E}_{wave} , so to get closer to a WWT regime. Yet, it is not sufficient since unstratified flows ($F_h \geq 1$) have almost no energy in waves modes (i.e. $E_{\text{wave}} \ll 1$). Increasing the stratification (decreasing F_h) is therefore required to reach that goal (Figure 13(a)), but it also tends to increase the vortical mode energy (Figure 3(a)) when they are not artificially removed from the dynamics. Figure 13(b) shows that \tilde{E}_{wave} tends to decrease with \mathcal{R} for sufficiently low F_h . This is consistent with the numerical simulations of stratified flows forced by tides [45], which show convincing signatures of a WWT regime at relatively small \mathcal{R} when compared to more usual strongly stratified simulations. However, some of our simulations at low F_h and high \mathcal{R} remain affected by hyper-viscosity, which prevent us to draw definitive conclusions on this point.

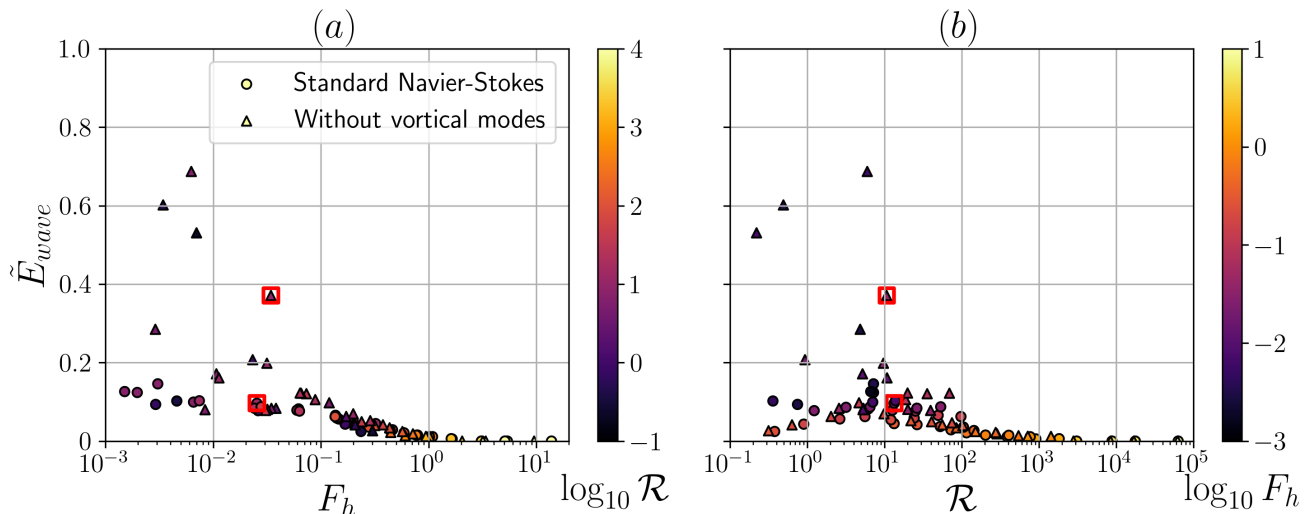


FIG. 13. \tilde{E}_{wave} as a function of F_h (a) and \mathcal{R} (b) for all our simulations with or without vortical modes. The red boxes indicate the simulations with $(N, \mathcal{R}_i) = (40, 20)$ investigated in the previous subsections.

IV. CONCLUSIONS

In this study, we performed direct numerical simulations of stratified turbulence without shear modes, and with or without vortical modes. We observed that removing vortical modes helps to have a better overall balance between poloidal kinetic energy and potential energy. However, the spatial spectra of kinetic and potential energy appear to behave very similarly for simulations with or without vortical modes.

We performed a spectral energy budget in the two-dimensional spectral space. We observed that the conversion between kinetic energy and potential energy did not show fluctuations around zero in our simulations, as we would expect for a system of statistically stationary waves. We also observe that the conversion between potential energy and kinetic energy becomes small when $\chi_d > 1$. Due to the anisotropy of stratified flows, this means that it exists a range where waves are efficiently dissipated by viscosity, but not necessarily the vortices.

A spatiotemporal analysis in the buoyancy range showed that removing vortical mode helps to concentrate the energy in temporal scales. However, increasing stratification is necessary to get approach a WWT regime. As in [19], we observed that waves are present in a region delimited by the non-linearity parameter $\chi_L \leq 1/3$ even when vortical modes are absent. We also observed evidences for the presence of slow waves ($k_z \gg k_h$) subject to TRI when $\chi_L \geq 1/3$. However, the non-linear broadening is shown to be large for $k_z \gg k_h$, therefore breaking a WWT theory's assumption in this region of the spectral space. This shows that the presence of vortical modes does not appear to be the only barrier to internal gravity waves turbulence in real flows.

Using a simple diagnostic to quantify wave's energy contained in a stratified flow, we showed that a WWT regime should be attained at very high stratification if the vortical modes are removed from the dynamics. Complementing earlier studies [45], our work suggests a subtle effect of the buoyancy Reynolds which should not be too large in order to observe a WWT regime. We plan to investigate such a regime in further studies.

ACKNOWLEDGMENTS

This project was supported by the Simons Foundation through the Simons collaboration on wave turbulence. Part of the computations have been done on the ‘‘Mesocentre SIGAMM’’ machine, hosted by Observatoire de la Cote d’Azur. The authors are grateful to the OPAL infrastructure from Universit e C te d’Azur and the Universit e C te d’Azur’s Center for High-Performance Computing for providing resources and support. This work was granted access to the HPC/AI resources of IDRIS under the allocation 2022-A0122A13417 made by GENCI.

Appendix A: Forcing scheme

The forcing used in our simulations is prescribed by the following algorithm:

```

t = 0: generate two random numbers  $f_{0\mathbf{k}}, f_{1\mathbf{k}} \sim \mathcal{P} \forall \mathbf{k}$  in the forcing region;  $t_0 = 0$ ;
while  $t \leq T$  do
   $t \rightarrow t + \delta t$ ;
  if  $t - t_0 \geq T_c$  then
     $t_0 \rightarrow t$ ;
     $f_{0\mathbf{k}} \rightarrow f_{1\mathbf{k}}$ ;
    generate  $f_{1\mathbf{k}} \sim \mathcal{P}$ 
  end
   $\hat{\mathbf{f}}_{\mathbf{k}} = \left\{ f_{0\mathbf{k}} - \frac{(f_{1\mathbf{k}} - f_{0\mathbf{k}})}{2} \left[ \cos \left( \frac{\pi(t - t_0)}{T_c} \right) + 1 \right] \right\} \mathbf{e}_{p\mathbf{k}}$ 
   $\hat{\mathbf{f}}_{\mathbf{k}}$  are normalized to ensure  $P_K = 1$ 
end

```

where \mathcal{P} is the probability law which has for distribution

$$p_X(x) = \begin{cases} \frac{1}{4} & \text{if } \text{Re}(x) \in [-1 : 1] \text{ and } \text{Im}(x) \in [-1 : 1] \\ 0 & \text{otherwise} \end{cases} \quad (\text{A1})$$

and δt is the time increment at each time step.

Appendix B: List of simulations

Control parameters				With vortical modes			Without vortical modes		
N	$\mathcal{R}_i = 1/\nu N^2$	n_h	n_z	$k_{\max}\eta$	F_h	\mathcal{R}	$k_{\max}\eta$	F_h	\mathcal{R}
0.25	64000	640	320	1.07	1.38e+01	63732	1.07	9.51e+00	62762
0.66	9000	640	320	1.09	5.37e+00	8868	1.10	3.38e+00	8487
0.66	18000	1280	640	1.29	5.09e+00	17751	1.30	3.18e+00	17025
1.12	3200	640	320	1.07	3.08e+00	3093	1.10	2.04e+00	2809
2	1000	640	320	1.09	1.65e+00	914	1.16	1.02e+00	719
2	2000	1280	640	1.30	1.62e+00	1834	1.38	9.41e-01	1436
3	450	640	320	1.10	1.08e+00	389	1.18	7.13e-01	288
3	900	1280	640	1.30	1.01e+00	773	1.42	6.04e-01	546
4	250	640	320	1.12	7.87e-01	204	1.21	5.70e-01	151
4	500	1280	640	1.33	7.67e-01	408	1.47	4.44e-01	276
5.20	150	640	320	1.13	5.89e-01	116	1.21	4.33e-01	85.7
6.50	100	640	320	1.11	4.61e-01	72.8	1.18	3.76e-01	56.2
6.50	200	1280	640	1.32	4.39e-01	144	1.43	3.16e-01	104
10	5	320	160	2.79	4.71e-01	3.4	2.85	5.83e-01	3.2
10	10	320	160	1.67	3.58e-01	6.7	1.71	4.33e-01	6.1
10	20	640	320	1.98	3.22e-01	13.4	1.03	3.45e-01	11.6
10	40	640	320	1.18	2.94e-01	26.5	1.24	2.87e-01	22.1
10	80	1280	640	1.41	2.84e-01	52.9	0.75	2.38e-01	40.8
10	160	1280	640	0.84	2.78e-01	106	0.91	2.03e-01	75.0
14.5	20	640	320	1.16	1.98e-01	12.2	1.22	1.99e-01	9.9
20	1	640	160	7.64	2.35e-01	0.4	8.00	3.01e-01	0.3
20	2	640	160	4.35	1.68e-01	0.9	4.75	2.07e-01	0.6
20	5	640	160	2.10	1.46e-01	2.6	2.24	1.71e-01	2.0
20	10	1280	320	2.47	1.35e-01	5.6	2.58	1.19e-01	4.7
20	20	1280	320	1.44	1.35e-01	11.9	1.53	8.85e-02	9.4
20	40	1280	320	0.85	1.40e-01	24.3	0.91	8.84e-02	18.8
20	80	1920	480	0.76	1.36e-01	49.6	0.55	7.32e-02	35.8
20	160	1280	320	0.30	1.35e-01	98.0	0.33	6.53e-02	69.5
30	10	1280	320	1.31	6.19e-02	6.2	1.39	3.63e-02	4.8
30	20	1920	480	1.16	5.97e-02	12.7	0.83	3.15e-02	9.7
30	40	1280	320	0.46	6.31e-02	25.2	0.49	6.39e-02	20.0
40	1	640	160	2.49	3.09e-02	0.5	2.70	4.64e-02	0.4
40	2	640	160	1.42	2.61e-02	1.2	1.52	2.32e-02	0.9
40	5	1280	320	1.42	2.58e-02	3.2	1.50	3.82e-02	2.6
40	10	1280	320	0.84	2.36e-02	6.5	0.88	3.46e-02	5.4
40	20	2560	640	0.99	2.54e-02	13.4	1.05	3.43e-02	10.7
40	40	1280	320	0.30	2.41e-02	26.3	0.32	3.18e-02	20.1
40	80	1280	320	0.18	2.78e-02	53.6	0.19	3.06e-02	39.6
60	10	1280	320	0.45	6.55e-03	7.1	0.48	1.07e-02	5.2
60	20	1280	320	0.27	7.42e-03	13.9	0.28	1.13e-02	10.8
80	0.5	640	80	1.37	4.58e-03	0.4	1.55	6.99e-03	0.2
80	1	640	80	0.81	2.92e-03	0.7	0.89	3.42e-03	0.5
80	10	2560	320	0.58	3.05e-03	7.2	0.63	8.38e-03	5.3
100	10	1280	160	0.21	1.97e-03	7.2	0.22	6.25e-03	6.0
120	10	1280	160	0.16	1.50e-03	6.7	0.17	2.90e-03	4.9

-
- [1] V. E. Zakharov, V. S. L'vov, and G. Falkovich, *Kolmogorov Spectra of Turbulence I*, Springer Series in Nonlinear Dynamics (Springer, 1992).
- [2] S. Nazarenko, *Wave Turbulence*, Lecture Notes in Physics, Vol. 825 (Springer, 2011).
- [3] S. Nazarenko, *Wave turbulence*, **56**, 359 (2015), publisher: Taylor & Francis .eprint: <https://doi.org/10.1080/00107514.2015.1015250>.
- [4] E. Falcon and N. Mordant, Experiments in surface gravity–capillary wave turbulence, **54**, 1 (2022), .eprint: <https://doi.org/10.1146/annurev-fluid-021021-102043>.
- [5] S. Galtier, S. V. Nazarenko, A. C. Newell, and A. Pouquet, A weak turbulence theory for incompressible magnetohydro-

- dynamics, **63**, 447 (2000), publisher: Cambridge University Press.
- [6] P. Caillol and V. Zeitlin, Kinetic equations and stationary energy spectra of weakly nonlinear internal gravity waves, **32**, 81 (2000).
- [7] S. Galtier, Weak inertial-wave turbulence theory, **68**, 015301 (2003), publisher: American Physical Society.
- [8] S. B. Medvedev and V. Zeitlin, Turbulence of near-inertial waves in the continuously stratified fluid, **371**, 221 (2007).
- [9] V. S. L'vov and S. Nazarenko, Weak turbulence of kelvin waves in superfluid he, **36**, 785 (2010), publisher: American Institute of Physics.
- [10] G. Düring, C. Josseland, and S. Rica, Weak turbulence for a vibrating plate: Can one hear a kolmogorov spectrum?, **97**, 025503 (2006), publisher: American Physical Society.
- [11] S. Galtier and S. V. Nazarenko, Turbulence of weak gravitational waves in the early universe, **119**, 221101 (2017), publisher: American Physical Society.
- [12] S. Dyachenko, A. C. Newell, A. Pushkarev, and V. E. Zakharov, Optical turbulence: weak turbulence, condensates and collapsing filaments in the nonlinear schrödinger equation, **57**, 96 (1992).
- [13] A. Griffin, G. Krstulovic, V. S. L'vov, and S. Nazarenko, Energy spectrum of two-dimensional acoustic turbulence, **128**, 224501 (2022), publisher: American Physical Society.
- [14] L. Biven, S. V. Nazarenko, and A. C. Newell, Breakdown of wave turbulence and the onset of intermittency, **280**, 28 (2001).
- [15] B. Miquel and N. Mordant, Nonstationary wave turbulence in an elastic plate, **107**, 034501 (2011), publisher: American Physical Society.
- [16] N. Yokoyama and M. Takaoka, Identification of a separation wave number between weak and strong turbulence spectra for a vibrating plate, **89**, 012909 (2014), publisher: American Physical Society.
- [17] Y. Pan and D. K. Yue, Direct numerical investigation of turbulence of capillary waves, **113**, 094501 (2014), publisher: American Physical Society.
- [18] Y. Zhu, B. Semisalov, G. Krstulovic, and S. Nazarenko, Testing wave turbulence theory for the gross-pitaevskii system, **106**, 014205 (2022), publisher: American Physical Society.
- [19] N. Yokoyama and M. Takaoka, Energy-based analysis and anisotropic spectral distribution of internal gravity waves in strongly stratified turbulence, **4**, 104602 (2019), publisher: American Physical Society.
- [20] N. Yokoyama and M. Takaoka, Energy-flux vector in anisotropic turbulence: application to rotating turbulence, **908**, A17 (2021), publisher: Cambridge University Press.
- [21] C. Staquet and J. Sommeria, INTERNAL GRAVITY WAVES: From instabilities to turbulence, **34**, 559 (2002), eprint: <https://doi.org/10.1146/annurev.fluid.34.090601.130953>.
- [22] G. K. Vallis, *Atmospheric and Oceanic Fluid Dynamics: Fundamentals and Large-Scale Circulation*, 2nd ed. (Cambridge University Press, 2017).
- [23] J. A. MacKinnon, Z. Zhao, C. B. Whalen, A. F. Waterhouse, D. S. Trossman, O. M. Sun, L. C. S. Laurent, H. L. Simmons, K. Polzin, R. Pinkel, A. Pickering, N. J. Norton, J. D. Nash, R. Musgrave, L. M. Merchant, A. V. Melet, B. Mater, S. Legg, W. G. Large, E. Kunze, J. M. Klymak, M. Jochum, S. R. Jayne, R. W. Hallberg, S. M. Griffies, S. Diggs, G. Danabasoglu, E. P. Chassignet, M. C. Buijsman, F. O. Bryan, B. P. Briegleb, A. Barna, B. K. Arbic, J. K. Ansong, and M. H. Alford, Climate process team on internal wave-driven ocean mixing, **98**, 2429 (2017), publisher: American Meteorological Society Section: Bulletin of the American Meteorological Society.
- [24] M. Gregg, E. D'Asaro, J. Riley, and E. Kunze, Mixing efficiency in the ocean, **10**, 443 (2018), eprint: <https://doi.org/10.1146/annurev-marine-121916-063643>.
- [25] P. Billant and J.-M. Chomaz, Self-similarity of strongly stratified inviscid flows, **13**, 1645 (2001), publisher: American Institute of Physics.
- [26] M. L. Waite and P. Bartello, Stratified turbulence dominated by vortical motion, **517**, 281 (2004), publisher: Cambridge University Press.
- [27] M. L. Waite and P. Bartello, Stratified turbulence generated by internal gravity waves, **546**, 313 (2006), publisher: Cambridge University Press.
- [28] E. Lindborg, The energy cascade in a strongly stratified fluid, **550**, 207 (2006), publisher: Cambridge University Press.
- [29] G. Brethouwer, P. Billant, E. Lindborg, and J.-M. Chomaz, Scaling analysis and simulation of strongly stratified turbulent flows, **585**, 343 (2007), publisher: Cambridge University Press.
- [30] M. L. Waite, Stratified turbulence at the buoyancy scale, **23**, 066602 (2011), publisher: American Institute of Physics.
- [31] Y. Kimura and J. R. Herring, Energy spectra of stably stratified turbulence, **698**, 19 (2012), publisher: Cambridge University Press.
- [32] P. Bartello and S. M. Tobias, Sensitivity of stratified turbulence to the buoyancy reynolds number, **725**, 1 (2013), publisher: Cambridge University Press.
- [33] A.-M. E. G. Brunner-Suzuki, M. A. Sundermeyer, and M.-P. Lelong, Upscale energy transfer by the vortical mode and internal waves, **44**, 2446 (2014), publisher: American Meteorological Society Section: Journal of Physical Oceanography.
- [34] P. Augier, P. Billant, and J.-M. Chomaz, Stratified turbulence forced with columnar dipoles: numerical study, **769**, 403 (2015), publisher: Cambridge University Press.
- [35] A. Maffioli, Vertical spectra of stratified turbulence at large horizontal scales, **2**, 104802 (2017), publisher: American Physical Society.

- [36] Y. V. Lvov and E. G. Tabak, Hamiltonian formalism and the garrett-munk spectrum of internal waves in the ocean, **87**, 168501 (2001), publisher: American Physical Society.
- [37] G. Dematteis and Y. V. Lvov, Downscale energy fluxes in scale-invariant oceanic internal wave turbulence, **915**, A129 (2021), publisher: Cambridge University Press.
- [38] G. Dematteis, K. Polzin, and Y. V. Lvov, On the origins of the oceanic ultraviolet catastrophe, **52**, 597 (2022), publisher: American Meteorological Society Section: Journal of Physical Oceanography.
- [39] A. Maffioli, A. Delache, and F. S. Godeferd, Signature and energetics of internal gravity waves in stratified turbulence, **5**, 114802 (2020), publisher: American Physical Society.
- [40] H. Lam, A. Delache, and F. S. Godeferd, Partitioning waves and eddies in stably stratified turbulence, **11**, 420 (2020), number: 4 Publisher: Multidisciplinary Digital Publishing Institute.
- [41] H. Lam, A. Delache, and F. S. Godeferd, Energy balance and mixing between waves and eddies in stably stratified turbulence, **923**, A31 (2021), publisher: Cambridge University Press.
- [42] C. Brouzet, Internal wave attractors : from geometrical focusing to non-linear energy cascade and mixing (2016).
- [43] G. Davis, T. Jamin, J. Deleuze, S. Joubaud, and T. Dauxois, Succession of resonances to achieve internal wave turbulence, **124**, 204502 (2020), publisher: American Physical Society.
- [44] C. Rodda, C. Savaro, G. Davis, J. Reneuve, P. Augier, J. Sommeria, T. Valran, S. Viboud, and N. Mordant, Experimental observations of internal wave turbulence transition in a stratified fluid, **7**, 094802 (2022), publisher: American Physical Society.
- [45] T. L. Reun, B. Favier, and M. L. Bars, Parametric instability and wave turbulence driven by tidal excitation of internal waves, **840**, 498 (2018), publisher: Cambridge University Press.
- [46] R. Meyrand, S. Galtier, and K. H. Kiyani, Direct evidence of the transition from weak to strong magnetohydrodynamic turbulence, **116**, 105002 (2016), publisher: American Physical Society.
- [47] T. Le Reun, B. Favier, A. J. Barker, and M. Le Bars, Inertial wave turbulence driven by elliptical instability, **119**, 034502 (2017), publisher: American Physical Society.
- [48] T. L. Reun, B. Favier, and M. L. Bars, Experimental study of the nonlinear saturation of the elliptical instability: inertial wave turbulence versus geostrophic turbulence, **879**, 296 (2019), publisher: Cambridge University Press.
- [49] M. Brunet, B. Gallet, and P.-P. Cortet, Shortcut to geostrophy in wave-driven rotating turbulence: The quartet instability, **124**, 124501 (2020), publisher: American Physical Society.
- [50] E. Monsalve, M. Brunet, B. Gallet, and P.-P. Cortet, Quantitative experimental observation of weak inertial-wave turbulence, **125**, 254502 (2020), publisher: American Physical Society.
- [51] S. Nazarenko, Verifying weak turbulence theory, **13**, 194 (2020), publisher: American Physical Society.
- [52] P. Müller, G. Holloway, F. Henyey, and N. Pomphrey, Nonlinear interactions among internal gravity waves, **24**, 493 (1986), eprint: <https://onlinelibrary.wiley.com/doi/pdf/10.1029/RG024i003p00493>.
- [53] Y. V. Lvov, K. L. Polzin, and N. Yokoyama, Resonant and near-resonant internal wave interactions, **42**, 669 (2012), publisher: American Meteorological Society Section: Journal of Physical Oceanography.
- [54] Y. V. Lvov, K. L. Polzin, E. G. Tabak, and N. Yokoyama, Oceanic internal-wave field: Theory of scale-invariant spectra, **40**, 2605 (2022), publisher: American Meteorological Society Section: Journal of Physical Oceanography.
- [55] C. H. McComas and F. P. Bretherton, Resonant interaction of oceanic internal waves, **82**, 1397 (1977), eprint: <https://onlinelibrary.wiley.com/doi/pdf/10.1029/JC082i009p01397>.
- [56] J. A. MacKinnon, M. H. Alford, O. Sun, R. Pinkel, Z. Zhao, and J. Klymak, Parametric subharmonic instability of the internal tide at 29°n, **43**, 17 (2013), publisher: American Meteorological Society Section: Journal of Physical Oceanography.
- [57] A. Craya, Contribution à l'analyse de la turbulence associée à des vitesses moyennes (1957).
- [58] Y. V. Lvov and N. Yokoyama, Nonlinear wave-wave interactions in stratified flows: Direct numerical simulations, **238**, 803 (2009).
- [59] L. M. Smith and F. Waleffe, Generation of slow large scales in forced rotating stratified turbulence, **451**, 145 (2002), publisher: Cambridge University Press.
- [60] J.-P. Laval, J. C. McWilliams, and B. Dubrulle, Forced stratified turbulence: Successive transitions with reynolds number, **68**, 036308 (2003), publisher: American Physical Society.
- [61] F. S. Godeferd, A. Delache, and C. Cambon, Toroidal/poloidal modes dynamics in anisotropic turbulence, in *Turbulence and Interactions, Notes on Numerical Fluid Mechanics and Multidisciplinary Design*, edited by M. Deville, T.-H. Lê, and P. Sagaut (Springer, 2010) pp. 151–158.
- [62] A. V. Mohanan, C. Bonamy, M. C. Linares, and P. Augier, FluidSim: Modular, object-oriented python package for high-performance CFD simulations, **7**, 14 (2019), number: 1 Publisher: Ubiquity Press.
- [63] M. C. Linares, Numerical study of 2d stratified turbulence forced by internal gravity waves (2020).
- [64] S. V. Nazarenko and A. A. Schekochihin, Critical balance in magnetohydrodynamic, rotating and stratified turbulence: towards a universal scaling conjecture, **677**, 134 (2011), publisher: Cambridge University Press.
- [65] S. S. Cerri, T. Passot, D. Laveder, P.-L. Sulem, and M. W. Kunz, Turbulent regimes in collisions of 3d alfvén-wave packets (2022), 2207.04301 [astro-ph, physics:physics].
- [66] C. Herbert, R. Marino, D. Rosenberg, and A. Pouquet, Waves and vortices in the inverse cascade regime of stratified turbulence with or without rotation, **806**, 165 (2016), publisher: Cambridge University Press.